2017

Effects of Strip Thickness and Damping on Flow-Induced Motions of a Circular Cylinder

Andrew John Auvil
Lehigh University

EFFECTS OF STRIP THICKNESS AND DAMPING ON FLOW-INDUCED MOTIONS OF A CIRCULAR CYLINDER

by

Andrew Auvil

A Thesis

Presented to the Graduate and Research Committee

of Lehigh University

in Candidacy for the Degree of

Master of Science

in

Mechanical Engineering

Lehigh University

May 2017

Certificate of Approval

This thesis is accepted and approved in partial fulfillment of the requirements for the Master of Science in Mechanical Engineering.

_____

Date Approved

_____

Dr. Arindam Banerjee
Thesis Advisor & Associate Professor,
Department of Mechanical Engineering & Mechanics
Lehigh University

_____

Dr. Gary Harlow
Department Chair Person
Department of Mechanical Engineering & Mechanics
Lehigh University

Acknowledgements

I would like to express my sincere, heartfelt gratitude to my thesis advisor, Dr. Arindam Banerjee, for his guidance, instruction, and support over the course of my Master's research. Special thanks are due to Ashwin Vinod for taking on the role of mentor to introduce me to the subject of flow-induced motion and provide invaluable insight into all aspects of this project. I am grateful to Richard Towne (Machinist, MEM) for his assistance in the design and manufacturing of the experimental apparatus. His expertise, insight, and advice contributed significantly to this project's success. I would also like to thank my fellow lab members: Zack Farley, Andy Bergey, Rinosh Polavarapu, Angela Lawrence, Rahul Raghavendra, Sudharsan Kalidoss, Matt Pasch, Saif Ali, and Pranav Modali for their help and support. Most importantly, I would like to thank my parents, Jane and Steve Auvil, for their unconditional love and support, without which none of this would have been possible.

Table of Contents

List of Figures

List of Tables

Abstract

Vortex-induced vibration (VIV) occurs as the flow around a bluff body, such as a cylinder, separates and causes the formation of vortices and a varied pressure distribution along the surface. Vortices are alternatingly shed, resulting in an alternating force on the body. VIV can have potentially destructive effects in structural applications, which prompted the majority of research to focus on mitigation and suppression efforts. Since the discovery of using vortex-induced vibration for energy harvesting by Bernitsas and group at the University of Michigan in 2005, researchers have begun to focus on augmentation mechanisms for VIV and galloping of circular cylinders for expanding energy harvesting capacity of the device. The current experimental work examines the effect of attaching smooth strips of varying thickness to a circular cylinder, as well as the effect of mass-damping for a given strip thickness, on its vibration response and power generation potential, and builds on previous work done by Vinod and Banerjee [1]. Five strip thicknesses ranging from 1.6% to 31% of the cylinder diameter were tested, along with three values of mass-damping. Each combination of thickness and damping experienced galloping at high flow velocities. Greater strip thickness resulted in a higher rate of increase of vibration amplitude with flow velocity, as well as a tendency to transition directly from VIV to galloping. Higher damping resulted in lower VIV amplitudes, a higher rate of increase in galloping amplitudes, lower vibration frequencies, and a lower Reynolds number range of synchronization. These observations show that higher strip thickness and lower damping lead to increased energy harvesting and power generation potential.

1 Introduction

1.1 Flow-Induced Motion

Flow-induced motion (FIM) is a common phenomenon which can have potentially devastating effects in numerous structural applications if not accounted for during the design process. The most common types of FIM are vortex-induced vibration (VIV), galloping, flutter, and buffeting [2]. Vortex-induced vibration (VIV) and galloping are commonly encountered in engineered structures including bridges, towers, heat exchangers, and offshore structures. Both phenomena are caused by flow separation; however, VIV is self-limiting, whereas galloping is not. Flutter is an FIM commonly seen in aircraft wings and, rather than being instigated by flow separation, is a self-excited oscillatory motion that occurs above a critical velocity which is dependent on stiffness and damping. High-frequency oscillatory FIM caused by free-stream turbulence is called buffeting and is also prevalent in aircraft wings and civil engineering applications. The types of FIM relevant to this work are VIV and galloping.

1.2 Vortex-Induced Vibration

Vortex-induced vibration (VIV) is a resonance-driven FIM resulting from flow separation as fluid flows around a bluff body, such as a cylinder. This behavior results in vortex formation which in turn changes the pressure distribution along the surface. Asymmetric vortex formation leads to vortex shedding and an alternating lift force transverse to the flow direction. The behavior of an elastically mounted cylinder in crossflow can vary depending on system parameters such as mass and natural frequency, as well as flow speed and Reynolds number regime.

Reynolds number (*Re*), defined as the ratio between inertial forces and viscous forces in a flow, plays a substantial role in governing VIV response due to the dependence of VIV on flow separation. For flow past a cylinder, Reynolds number is given by:

$$Re = \frac{UD}{\nu} \tag{1}$$

where U is the flow velocity, D is the cylinder diameter, and υ is the kinematic viscosity of the fluid. The characteristics of flow around a fixed cylinder in different Reynolds number regimes are shown in Figure 1.1. At extremely low values of *Re*, the flow around a cylinder will not separate. A slight increase in *Re* results in the formation of a fixed vortex pair in the near wake, followed by the development of a laminar von Karman vortex street in the range $40<Re<150$. As *Re* increases, the wake transitions and results in a turbulent vortex street for $300<Re<3\times10^5$. This range can be broken up into three subdivisions of transition in the shear layer (TrSL). TrSL1 ranges from $300<Re<1.5\times10^3$ and involves the development of transition waves in the free shear layer. TrSL2 spans $1.5\times10^3<Re<3\times10^4$ where the formation of transition vortices in the free shear layer occurs. The range of $3\times10^4<Re<3\times10^5$ is classified as TrSL3, where the shear layer is fully turbulent [3]. The Reynolds number regime where VIV occurs depends on several system parameters including mass, damping, stiffness, and cylinder diameter. The work presented here was primarily conducted within the TrSL2 regime, reaching a maximum Reynolds number of $\sim4\times10^5$ in a select few cases.

The time-averaged and fluctuating lift and drag coefficients, C_L, C_L', C_D, and C_D', for a circular cylinder in the various Reynolds number regimes are shown in Figure 1.2. C_D is made up of two components: skin friction (C_{Df}) and pressure (C_{DP}). Skin friction

drag is high in the laminar flow regime and quickly decreases with increasing *Re* as viscous effects become less prominent. C_{DP} remains relatively high throughout TrSL and decreases near the beginning of the TrBL regime. It can also be seen from the figure that C_L' is always greater than C_D'. The majority of research into VIV has been conducted in the TrSL2 regime marked by a continuously increasing fluctuating lift coefficient.

The frequency of vortex shedding from a cylinder is defined by the Strouhal number (*St*):

$$St = \frac{f_{v0} D}{U} \tag{2}$$

where f_{v0} is the vortex-shedding frequency in Hz. For subcritical flows, spanning the range of $3\times10^2<Re<2\times10^5$, $St \sim 0.2$ [3, 4], indicating that the vortex shedding frequency increases linearly with flow velocity. At flow velocities where f_{v0} is close to f_n, large-amplitude vibrations occur in what is called "synchronization" or "lock-in".

The pattern of vortex shedding has been shown to differ with changes in proximity to lock-in [5], as shown in Figure 1.3a. Figure 1.3b shows the various modes of vortex-shedding that can be seen in VIV. The initial branch has been shown in experimental and numerical studies to be characterized by the 2S vortex shedding mode, where two single vortices are shed per oscillation cycle [6, 7]. Cylinders can undergo 2S, 2P or P+S vortex shedding during lock-in depending on system parameters. In the 2P mode, two vortex pairs are shed per cycle, whereas P+S consists of one pair of vortices and one single vortex being shed per cycle.

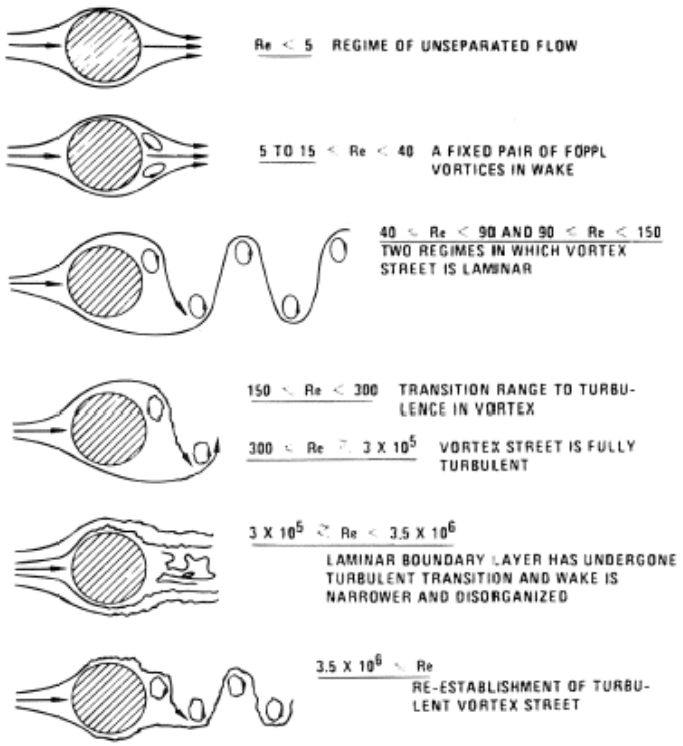

Figure 1.1 Wake behavior of flow past a cylinder in various Reynolds number regimes adapted from Lienhard [8]

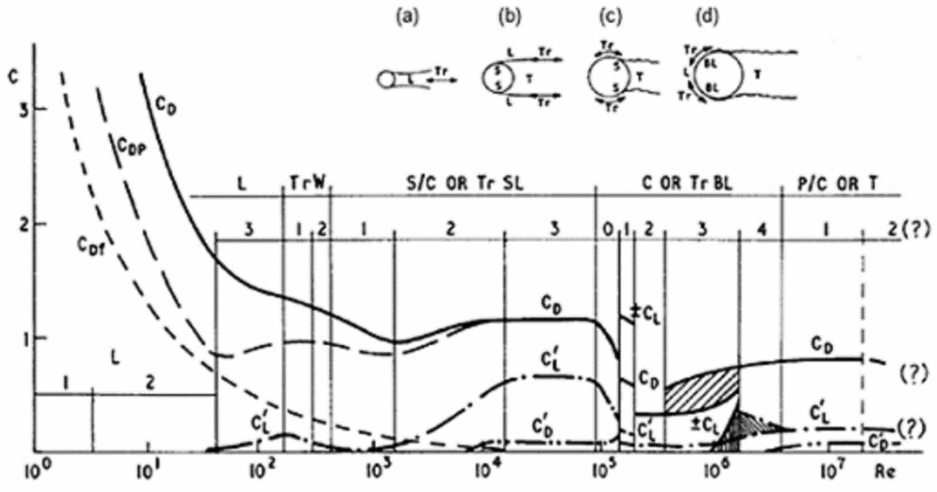

Figure 1.2 Force coefficients vs. Reynolds number over a range of flow regimes (adapted with permission from Zdravkovich, *Flow Around Circular Cylinders: Volume 1: Fundamentals* [3])

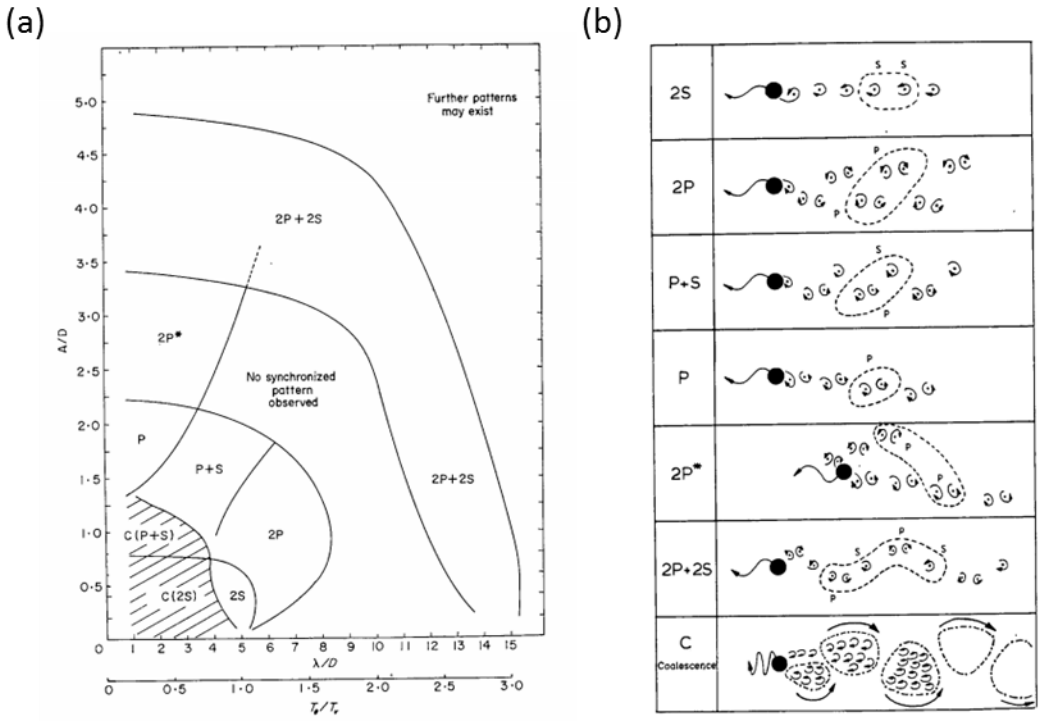

Figure 1.3 (a) Williamson-Roshko map for VIV; (b) Vortex shedding modes observed during VIV [5]

1.3 Mathematical Modeling

The equation for a mass-damper-spring system of mass *m*, damping *c*, and stiffness *k* subject to a forcing function is given by:

$$m\ddot{x} + c\dot{x} + kx = F(t) \tag{3}$$

where

$$c = 2\xi\sqrt{mk} \tag{4}$$

In VIV, the force *F* on the system is the alternating lift force F_L due to flow separation around the cylinder. From this equation, we can see that displacement is a function of the system mass, damping, stiffness, and lift force, where F_L is dependent on *Re* [9]. In the study of VIV, mass and damping are typically combined into one mass-damping term represented as the product of the mass ratio *m** (mass of the system over the mass of the displaced fluid) and the damping ratio ζ.

Several non-dimensional parameters are typically used to classify and quantify VIV response and are presented in Table 1.1. The mass ratio *m** is a ratio of the total moving mass of the system, *m*, to the mass of the displaced fluid, calculated using fluid density ρ, cylinder diameter *D*, and cylinder length *L*. Damping is quantified by the damping ratio, which is a function of damping constant *c*, spring stiffness *k*, moving mass, and added mass m_a which, for a cylinder, is the displaced fluid mass. Flow velocity *U* is non-dimensionalized as reduced velocity by dividing by the cylinder diameter and system natural frequency f_n. Amplitude and frequency are non-dimensionalized by the cylinder diameter and natural frequency respectively. Lift and drag coefficients are dependent on lift and drag forces F_L and F_D.

Table 1.1 Non-dimensional parameters used in this work

Parameter	Symbol	Definition
Mass Ratio	m^*	$4m/\pi\rho D^2 L$
Damping Ratio	ζ	$c/2\sqrt{k(m+m_a)}$
Reduced Velocity	U^*	$U/f_n D$
Amplitude Ratio	A^*	A/D
Frequency Ratio	f^*	f/f_n
Reynolds Number	Re	UD/ν
Strouhal Number	St	Df_{vo}/U
Lift Coefficient	C_L	$2F_L/\rho U^2 D$
Drag Coefficient	C_D	$2F_D/\rho U^2 D$

1.4 VIV Experiments

There have been numerous studies carried out over the years investigating all response characteristics of VIV in various types of bluff bodies in both air and water. Reviews by Sarpkaya [10, 11], Williamson and Govardhan [12], and Bearman [13] discuss many of the important studies conducted in this field that have improved our understanding of the how, why, and in what manner VIV can occur.

1.4.1 Effect of mass-damping and stiffness

The mass-damping parameter has been shown to impact VIV amplitude response and lock-in regime. For cases of very low mass-damping, Khalak and Williamson [14] showed that three distinct branches, initial, upper, and lower, are present in the amplitude response. At low flow velocities, an initial branch consisting of low-amplitude, sporadic vibrations is observed. As flow velocity increases and the vortex shedding frequency approaches the natural frequency of the oscillating system, high-amplitude vibrations can occur with an oscillation frequency approximately equal to f_n, referred to as the upper branch. These amplitudes are typically on the order of one diameter for an elastically mounted cylinder. As flow velocity increases further, vortex shedding frequency increases past the system natural frequency resulting in a decrease in amplitude and decrease in uniformity of vibration response. At high velocities, a smooth cylinder will only exhibit random, small-amplitude vibrations in what is called desynchronization. These observations contrast with the results by Feng who used a system with very high mass-damping. His experiments showed only an initial and lower branch response and no upper branch. The comparison of Williamson and Feng's results is presented in Figure 1.4. Klamo et al. [9] performed a set of experiments measuring the change in VIV

response over a wide range of damping ratios. The response of the lowest and highest damping cases reflects the results presented by Williamson and Feng [14] respectively. As damping is increased, decreasing upper and lower branch amplitudes and shorter excitation regions are observed.

Lee and Bernitsas [15] conducted a comprehensive study on the effects of varying damping at a constant spring stiffness, and varying stiffness at constant damping. This was done using their virtual V_{CK} system which can control the damping and stiffness of the system by means of a feedback loop, allowing them to easily test the independent effects of stiffness and damping in a systematic, controlled fashion [16]. They found that increases in damping for a given spring stiffness (Figure 1.5a) resulted in lower VIV amplitudes and a shorter range of excitation. The transition from initial branch to upper branch also becomes more gradual. At higher values of spring stiffness, increased damping is observed to push the peak upper branch amplitude to lower flow velocities, resulting in a more gradual transition to desynchronization. Figure 1.5b shows the variation in response with increasing stiffness at a constant damping. As stiffness increases, synchronization is pushed to higher velocities, upper branches increase in length, and maximum amplitude experienced in the upper branch increases. The upper branch is followed almost immediately by desynchronization, occurring more rapidly with increasing spring stiffness. The authors noted that although increased stiffness pushes the response to higher Reynolds numbers, it occurs in approximately the same U^* range regardless of stiffness.

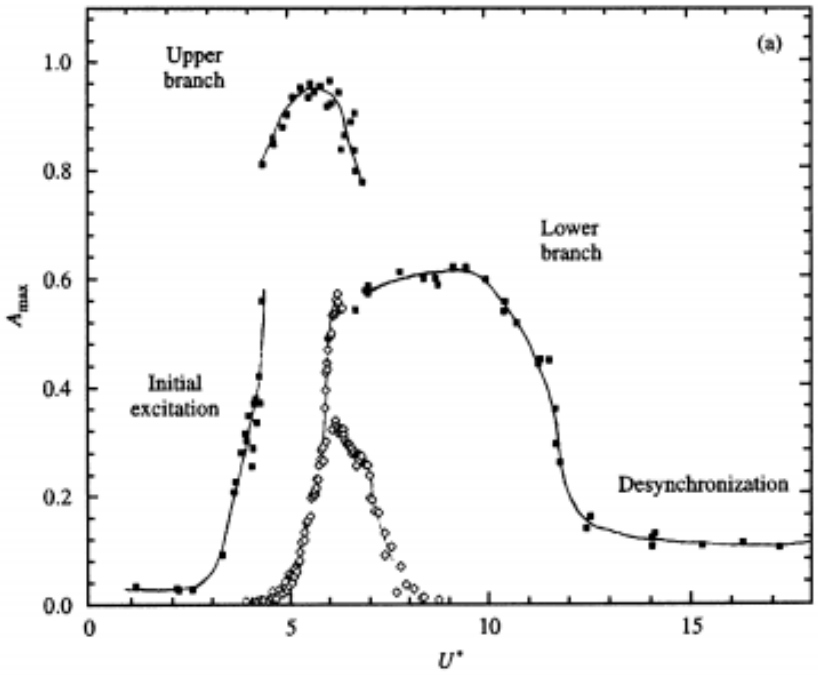

Figure 1.4 Amplitude response of circular cylinders (adapted from Williamson and Feng [14])

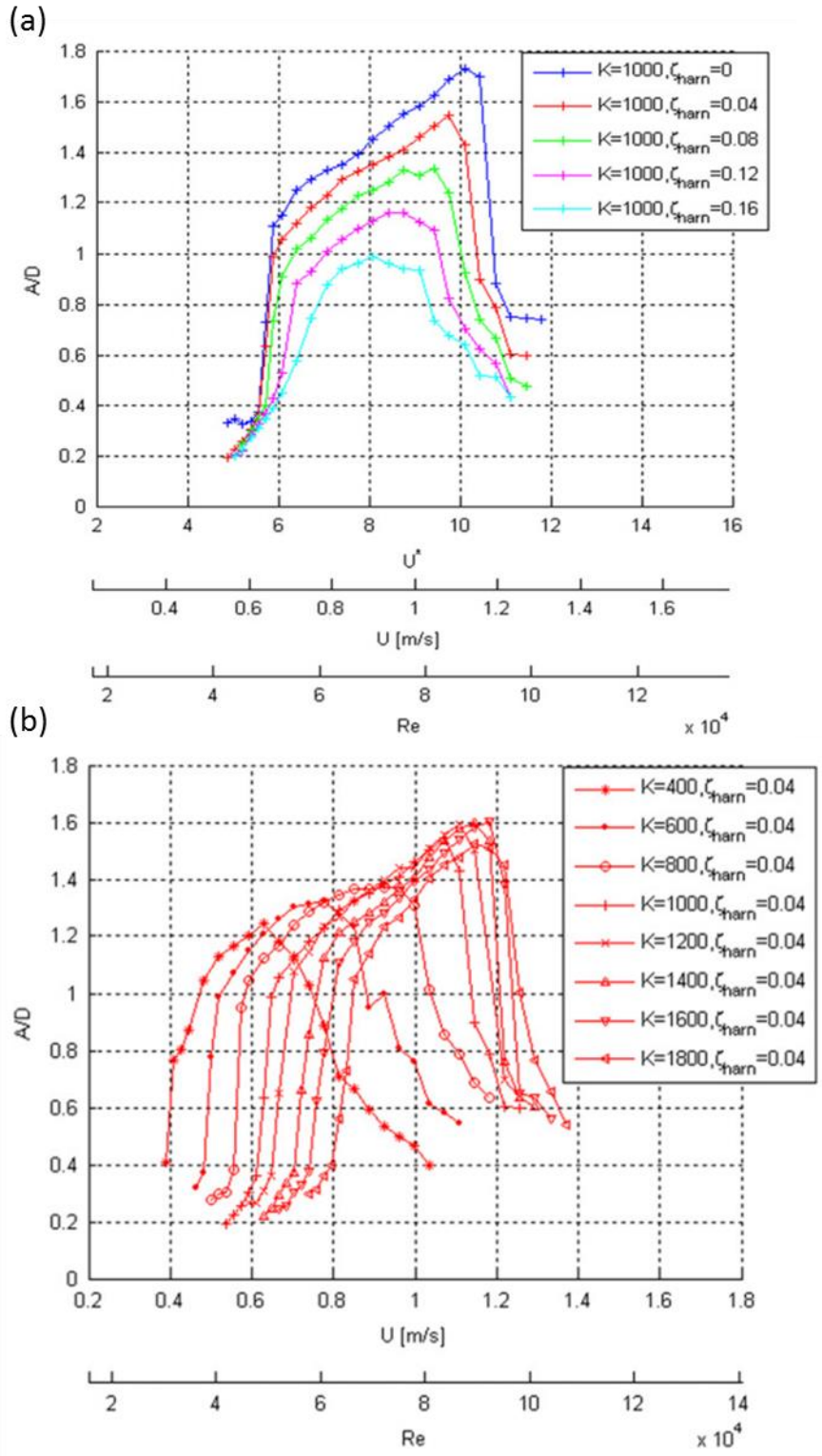

Figure 1.5 Amplitude response reported by Lee and Bernitsas for (a) constant stiffness, varying damping (b) constant damping, varying stiffness [15]

1.4.2 Effect of Reynolds number

Reynolds number was shown by Raghavan and Bernitsas [17] to have a strong effect on the VIV response of circular cylinders. Reynolds number regime of synchronization can be altered by changing the cylinder diameter or shifting the natural frequency of the system by modifying spring stiffness. The majority of VIV research has been conducted in the TrSL2 Reynolds number regime, with Bernitsas and his group operating primarily in TrSL3. Within TrSL3, the lower branch of response essentially disappears, and desynchronization occurs directly following the upper branch. As *Re* increases within this regime, the upper branch response goes from the rounded shape typically seen in TrSL2 to a linearly increasing upper branch of increasing width. The cylinder also undergoes 2P vortex shedding starting in the initial branch, different from what is predicted by the Williamson-Roshko plot in Figure 1.3a, which was developed based on measurements taken in the TrSL2 regime.

1.5 Galloping

A bluff body with cross-sectional asymmetry can undergo a motion called galloping at sufficiently high Reynolds numbers. Asymmetry is necessary to incite galloping, meaning this phenomenon can never be seen with a smooth, circular cylinder. Galloping, unlike VIV, is not resonance-driven and will increase boundlessly with flow velocity until structural failure occurs. Certain cases exhibit all three VIV branches before galloping oscillations begin, while others transition straight to galloping from the upper branch, depending on system parameters. Galloping can be categorized as hard (requiring a threshold amplitude) or soft (not requiring a threshold amplitude).

1.6 Experiments on Galloping

The effect of geometry on galloping has been examined in several studies using non-circular cylinders at various angles of attack. Mannini [18] gives a comprehensive review of experiments on the galloping response of rectangular cylinders of various aspect ratios. Cylinders with an aspect ratio of 3:2, in particular, were shown to exhibit high amplitude galloping oscillations over a wide range of mass-damping values. Weaver [19] found semicircular and parabolic cylinders to exhibit hard or soft galloping, depending on specific geometry. Alonso [20] performed experiments on the galloping response of elliptical cylinders at various angles of attack.

The effect of surface geometry modifications on the galloping of circular cylinders has also been investigated. Assi and Bearman [21] incited galloping using both solid and porous, non-rotating, splitter plates. In all cases tested, the excitation regime was delayed to higher flow velocities compared to a smooth cylinder, but vibration amplitudes proceeded to increase continuously as velocity increased. Force measurements and flow visualization show that the high amplitude vibrations are due to the reattachment of the separated shear layer to the plate tips.

Chang and Bernitsas [22] attached pairs of rough strips to a circular cylinder at various angles to influence VIV and galloping response. The use of rough strips is referred to as Passive Turbulence Control (PTC) by Bernitsas' group. They found that strips of various roughness levels attached at angles between 20° and 64° result in suppressed VIV response followed by galloping oscillations. Galloping did not occur for angles greater than 64° or lower than 16°. For a given strip location, coarser roughness had little effect on VIV but resulted in a faster increase in galloping amplitude. At a

given roughness level, varying strip angle between the limits of 64° to 16° resulted in higher VIV amplitudes and higher slope in galloping response.

A more extensive study on the effect of rough strips was conducted by Park and Bernitsas [23]. Figure 1.6 shows the PTC-to-FIM maps developed by this group for roughness using P180 and P60 sandpaper strips, indicating strip locations resulting in weak and strong suppression (WS, SS), hard galloping (HG) and soft galloping (SG) within TrSL3. The leftmost point on each circle is the frontal stagnation point of the cylinder. Both hard galloping zones required a threshold amplitude of roughly one diameter to transition to galloping. For both roughness levels, HG1 sees a wider upper branch and higher galloping amplitudes than HG2. In the soft galloping zone, angles below 30° show earlier transition to galloping with increasing strip placement angle, whereas transition to galloping is delayed with increasing angle for α>40°. For all galloping zones, suppressed VIV amplitudes were observed, and higher harmonic frequencies were seen in the frequency response.

Sun et al. [24] applied PTC to circular cylinders and performed extensive tests on the effect of mass, damping, and stiffness on VIV and galloping response in the TrSL3 regime. For a given m^* and ζ, lower spring stiffness resulted in higher amplitudes at a given *Re*. For a given stiffness and mass ratio, higher damping led to lower VIV and galloping amplitudes, as well as a lower-amplitude transition region. Increased damping also resulted in slightly lower oscillation frequencies during VIV and galloping.

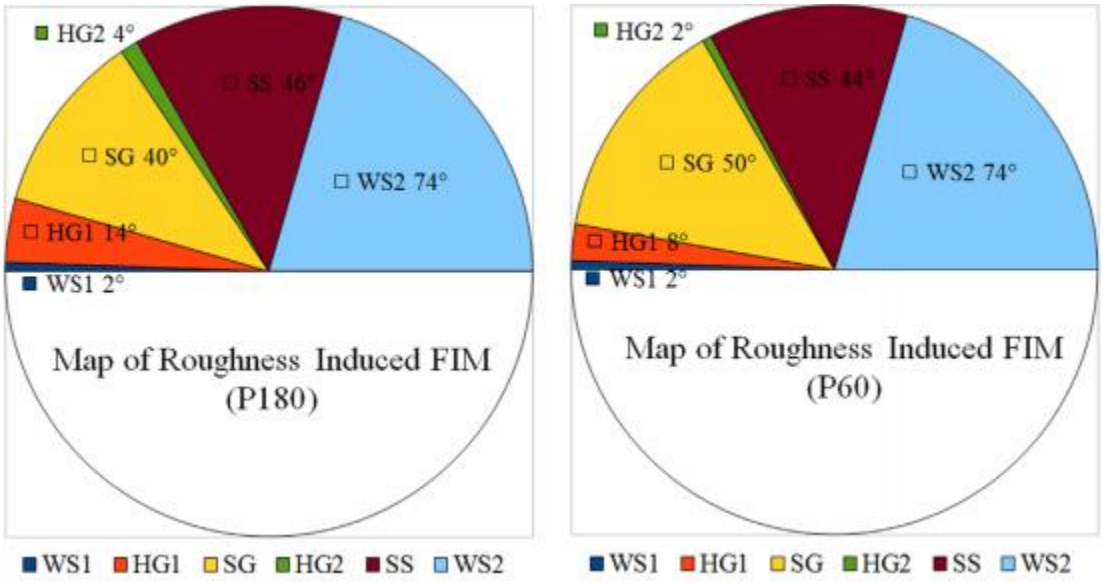

Figure 1.6 PTC-to-FIM maps based on experimental data by Park and Bernitsas [23] for two levels of roughness

Vinod and Banerjee [1] tested cylinders with various pairs of rough and smooth strips attached at angles varying from 60° to 100° with respect to the frontal stagnation point. Experiments were conducted entirely within the TrSL2 flow regime, whereas similar studies by Bernitsas' group presented above were conducted primarily in the TrSL3 regime. For a constant roughness level, a strip location of 60° resulted in higher VIV amplitude response as well as a transition to galloping, while strip locations of 80° and 100° suppressed VIV. All roughness levels tested resulted in increased VIV upper branch amplitudes and transition to galloping for an angle of 60°. However, finer grit size led to a shorter-lasting upper branch and lower amplitudes seen in the transition from VIV to galloping. All strip cases at 60° saw the frequency ratio maintain a relatively constant value of ~1 for the duration of galloping. A smooth strip pair of the same width and thickness was also tested at 60°. This configuration resulted in lower VIV amplitudes and a longer transition to galloping but showed higher galloping amplitudes at a significantly higher frequency than that achieved with rough strips. Higher frequency galloping response implies increased power generation potential compared to the other configurations tested in the TrSL2 regime.

1.7 Engineering Impact of VIV and Galloping

VIV and galloping are a cause for concern in many structural applications, including the design of bridges, skyscrapers, chimneys and smokestacks, power lines, and oil risers, due to their potentially destructive nature [11, 25]. It is imperative in civil engineering applications to take into account factors such as natural frequencies of structures and components and typical wind or current speeds so that resonance-based vibration, like VIV, can be avoided. In some cases, structures which would not normally

be subject to significant vortex-induced vibration may undergo destructive galloping oscillations due to a change in geometry. Specific examples include iced cables [26] and oil risers with significant marine life growth [27]. Due to the destructive nature of galloping, the primary research focus has historically been on identifying the conditions that cause galloping to occur so that it could be avoided. Extensive research has also been conducted over the last century to identify methods to suppress VIV to reduce the risk of structural failure.

1.8 VIV Suppression

Numerous attempts have been made to suppress VIV in cylinders by altering the geometry of the surface and near wake. Zdravkovich [28] compiled a review of studies that investigate various suppression mechanisms including surface protrusions, shrouds, and near-wake stabilizers. Surface protrusions include helical strakes [29], wires [30], and fins [31], which all work to alter the separation point and behavior of the separated shear layer. Various types of shrouds [32-36] suppress VIV by adversely affecting the entrainment layer where surrounding fluid necessary for vortex growth is brought towards the cylinder. Near-wake stabilizers include sawtooth fins [37], splitter plates [38], and guide vanes [39], and work to disrupt the interaction between entrainment layers on opposite sides of the cylinder, thereby suppressing vibration.

Park et al. [40] used localized surface roughness to suppress VIV amplitude response. Strong suppression resulting in more than a 30% reduction in peak amplitude, as well as a decrease in synchronization range, was seen for strip locations of $60° < \alpha < 106°$ with P180 roughness. In weaker suppression zones, the amplitude remained similar in shape to that of a smooth cylinder, but with a scaled down amplitude response.

Flow visualization measurements showed that vortex formation occurred over a longer length and resulted in smaller vortices being shed.

Sui et al. [41] tested the VIV suppressing ability of a variety of pitch angles, heights, and coverage lengths of helical strakes. Orientations with strakes spanning the length of the cylinder completely suppressed VIV to the point where there were no identifiable branches in the amplitude response. A 98% suppression was achieved at the reduced velocity corresponding to the peak upper branch amplitude of a smooth cylinder. Decreasing strake height was also shown to improve suppression, but to a lesser extent. The addition of strakes was able to suppress the vortex structures in the wake by altering separation points and disrupting shear layer interactions.

Over the last decade, a new concept has emerged which broadened the scope of research and shifted some focus away from suppression. The energy transferred from a flow to an elastically mounted bluff body could potentially be harnessed and used as a source of power. Since the introduction of this concept in 2005, several studies have been conducted on mechanisms that could be used to augment VIV for the purpose of energy harvesting.

1.9 Marine Hydrokinetic Energy

Marine hydrokinetic (MHK) energy refers to energy extracted from rivers, ocean currents, and waves. Available energy in tides and currents is estimated at 22,000 TWh/yr, and the annual consumption of energy worldwide is roughly 132,000 TWh [42], meaning that tapping into this energy source could provide vast improvements in the efficiency and environmental impact of our energy usage. Table 1.2 presents available power in rivers within the United States, as well as the theoretically recoverable power

from those sources based on a 2012 study by the Electric Power Research Institute [43]. The values presented are based on the use of available technologies at the time of the study, mainly hydrokinetic turbines. The majority of rivers are under 2 kn (1 m/s), slower than ideal for turbines which typically require 5-7 kn (2.5-3.5 m/s) to be financially practical [42]. Excitation ranges for vortex-induced vibration of circular cylinder systems capable of harvesting practical amounts of energy can be near or below 1 m/s depending on system parameters [44], prompting researchers to investigate the potential of harvesting energy from VIV.

Table 1.2 Theoretical available power in major rivers in the United States (adapted from [43])

Hydrologic Region	**Theoretical Power (Annual Energy, TWh/yr)**	**Technically Recoverable Power (Annual Energy, TWh/yr)**
New England	14.4	0.2
Mid-Atlantic	33.5	1.0
South Atlantic Gulf	38.5	1.2
Great Lakes	6.2	0.01
Ohio	79.2	6.9
Tennessee	20.4	1.0
Souris-Red-Rainy	1.8	0.03
Upper Mississippi	47.0	5.1
Lower Mississippi	208.8	57.4
Texas Gulf	8.9	0.05
Arkansas Red	45.1	1.3
Lower Missouri	79.8	5.6
Upper Missouri	74.3	2.8
Rio Grande	29.5	0.3
Lower Colorado	57.6	3.9
Upper Colorado	46.9	1.1
Great Basin	6.9	0
California	50.9	0.7
Pacific Northwest	296.7	11.0
Alaska	235	20.5
Total	1,381	119.9

1.10 VIVACE

The Vortex-Induced Vibration for Aquatic Clean Energy (VIVACE) converter was developed by Dr. Michael Bernitsas and his group at the University of Michigan in 2005 as a way to harness energy from slow-moving flows [44]. It makes use of the ability of cylinders to exhibit high-amplitude vibrations at low flow velocities, allowing these devices to tap into river and tidal currents which can be too slow for more conventional energy harvesting methods. Since the conceptualization of VIVACE, several studies have been conducted by Bernitsas' group [17, 22-24, 45-47] to augment VIV and galloping amplitude response and increase excitation range to allow for maximum energy extraction, resulting in increased power generation potential.

1.11 Motivation

The research presented here is motivated by the desire to contribute to the knowledge base of VIV and galloping augmentation mechanisms with application to marine hydrokinetic energy harvesting. The primary motivation for the specific test cases comes from the findings of Vinod and Banerjee [1]. They determined that a pair of smooth strips attached at an angle of 60° from the frontal stagnation point lead to higher amplitude, higher frequency galloping oscillations than any other cases tested in the TrSL2 regime. This work seeks to build on Vinod's work to investigate ways to improve upon what is currently the most efficient energy harvesting configuration for this flow regime.

2 Methods

2.1 Apparatus

Experiments were performed in Lehigh University's Model No. 505 Water Tunnel from Engineering Laboratory Design in Minnesota. The test section measures 24" × 24" × 79" (0.61 m × 0.61 m × 2 m) and can generate flow speeds of up to 0.95 m/s. Due to structural concerns stemming from excessive flutter of the cylinder, only velocities up to 0.71 m/s were used.

The experimental apparatus, shown in Figure 2.1, is designed to allow the cylinder to oscillate only transverse to the flow direction. The cylinder is attached to the bottom of an acrylic plate which is supported by four NewWay Inc. air bearings. This allows the plate to move along two 1" diameter stainless steel shafts attached to the aluminum frame. A compressed air supply line is connected to the air bearings and provides an air pressure of 80 psi. Slotted angle struts were attached to the frame and fitted with hooks to connect extension springs to the traversing plate. For an elastically mounted system, the use of springs is required to give the system a defined, measurable stiffness to be able to characterize the motions undergone by the cylinder. Acrylic mounts were designed and attached above the air bearings to join the body of the LVDT to the moving plate. The LVDT core rod was fixed in place using #4-40 threaded rods screwed into the core rod and attached to supports extending out from the apparatus frame. The support mounts were designed with slots to allow for horizontal and vertical adjustment to ensure minimal friction between the core rod and body. Steel struts extend outwards in line with the LVDT, onto which the adjustable angle bracket supports were mounted. The core rod-extension rod system was pulled taut and aligned to reduce

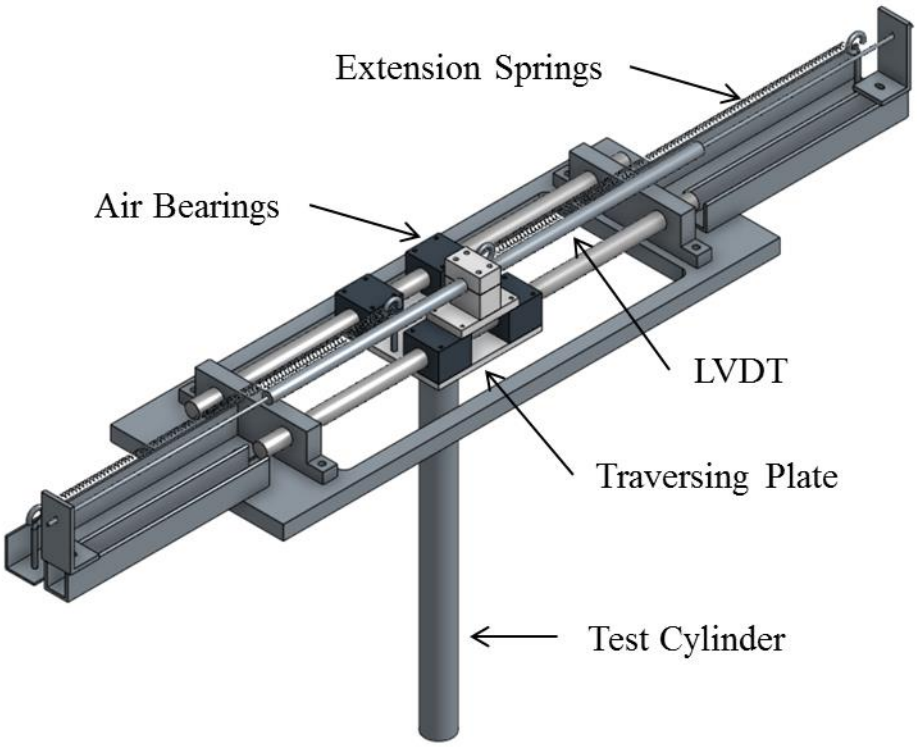

Figure 2.1 Experimental Apparatus at Lehigh University

frictional damping to its lowest possible level. Proper alignment of the LVDT body and core rod system was verified before each experiment. Appendix A provides more information about the design process of the LVDT mounting system.

The cylinder used in these experiments is a 22" (0.762m) section of 1.9" (0.0483m) diameter PVC pipe. With a tunnel width of 24" (0.61m), the blockage ratio is 7.9%, well below the threshold of 14%, where blockage effects begin to alter VIV and galloping response [48]. The cylinder is fitted with acrylic end caps to seal it from the water and to facilitate attachment of the cylinder to the traversing plate.

2.2 Diagnostics

A TE Connectivity SE750-20000-200 linear variable differential transformer (LVDT) was used to track cylinder displacement (see Appendix B for details). An LVDT translates the relative motion between the core and body into an electric signal which is linearly proportional to the displacement. The model employed here has a linearity error of 0.10% of the full-scale output, corresponding to ±0.02 inches. The LVDT was wired to a USB-6003 DAQ from National Instruments, which connects to the computer via USB. A LabVIEW script (Appendix D) was created to acquire the displacement data from the DAQ system at a frequency of 10 samples per second for a duration of 2 minutes. The raw data was then exported to Excel and processed in a MATLAB script, shown in Appendix E.1.

The damping ratio (ζ) of the oscillating system was determined through a series of tests. The plate was released at its maximum displacement from center and allowed to oscillate freely. The motion was recorded using LabVIEW for 30 seconds for each trial. A MATLAB script (Appendix E.2) was used to find the peaks of the displacement trace

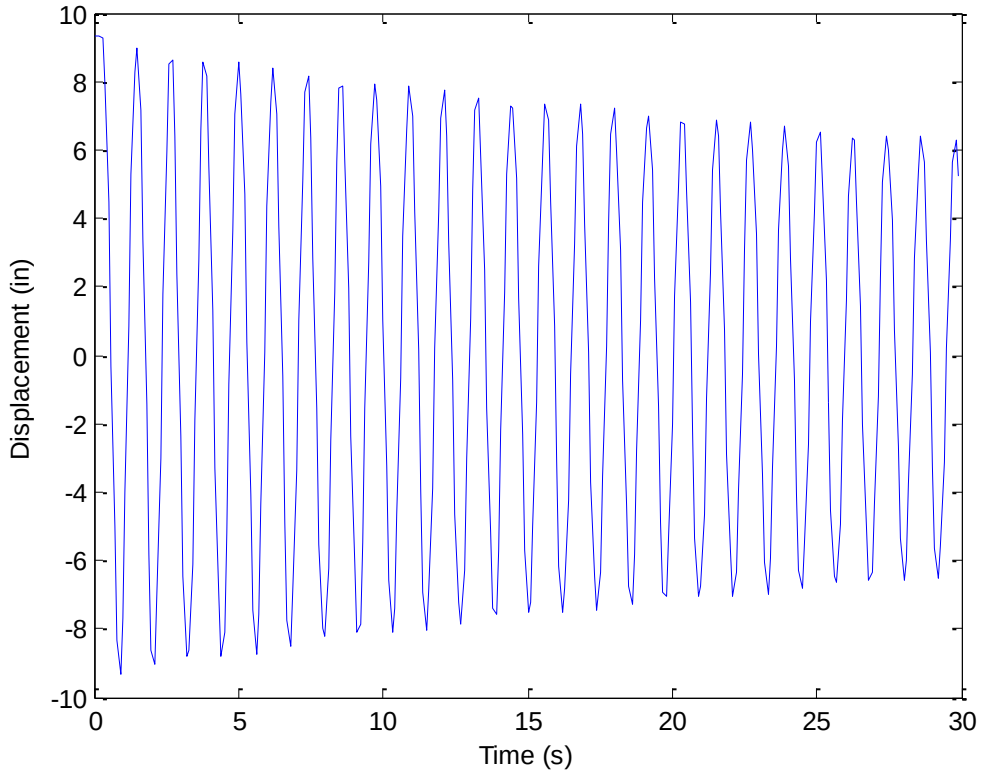

Figure 2.2 Displacement trace from damping test

(see Figure 2.2) and use the logarithmic decrement method to calculate the damping ratio. Relevant equations are shown below:

$$\delta = \frac{1}{n} \ln \frac{x_0}{x_n} \tag{5}$$

$$\xi = \frac{\delta}{\sqrt{4\pi^2 + \delta^2}} \tag{6}$$

$$\xi = \frac{c}{2\sqrt{k(m + m_a)}} \tag{7}$$

where δ is the logarithmic decrement and n is the nth peak in the displacement trace.

2.3 Test Cases

Two parameters were varied for these experiments to identify their effect on VIV and galloping responses: strip thickness and damping. Smooth tape strips of thickness of h = 787 μm (0.031") and width of 0.0127 m (0.5") were attached to the cylinder at an angle of 60° from the frontal stagnation point. This was shown to be the optimal angle to incite high amplitude galloping with smooth strips in the TrSL2 Reynolds number regime [1]. Multiple strips were attached one on top of another to vary strip thickness. A list of strip thicknesses used in this study is shown in Table 2.1. The system damping was controlled by varying spring stiffness. Three pairs of custom-made, music wire springs from W.B. Jones Springs Inc. were used, with equivalent stiffness values of 8.2 N/m, 33.4 N/m, and 81.4 N/m. The restoring force of these springs was assumed to vary linearly with the displacement. Table 2.2 lists the damping and natural frequency values associated with the three spring pairs used. All strip thicknesses were tested at one constant damping value. The effect of mass-damping was assessed using the plain

cylinder and strip thickness ratios of 8.2% and 24.5%. Twelve total cases were tested, as shown in Table 2.3.

Table 2.1 Strip thickness cases used in this study

Number of strips	**Thickness, H (mm)**	**H/D**
1	0.787	1.6%
5	3.935	8.2%
10	7.870	16.3%
15	11.805	24.5%
19	14.953	31%

Table 2.2 Spring stiffnesses and damping parameters for springs used

Spring Stiffness, k (N/m)	**Damping Ratio, ζ**	**Damping Constant, c**	**Natural Frequency, f_n (hz)**
k = 81.4	0.015	0.163	0.656
k = 33.4	0.026	0.175	0.420
k = 8.2	0.075	0.256	0.209

Table 2.3 Experimental cases

Case #	**$m^*\zeta$**	**H/D (%)**
0	0.015	0
1		1.6
2		8.2
3		16.3
4		24.5
5		31
6	0.026	0
7	0.075	
8	0.026	8.2
9	0.075	
10	0.026	24.5
11	0.075	

3 Results and Discussion

The variations in the response of the cylinder due to changes in strip thickness are discussed in terms of vibration amplitude, dominant frequency, displacement trace, and frequency spectra. The effect of increasing mass-damping for a given strip thickness is also discussed. A qualitative assessment is carried out based on oscillation velocities observed during the experiments to illustrate the power extraction potential of the different cases tested.

3.1 FIM of Circular Cylinder Attached with Strips

The response of the plain cylinder used in the current work, Case 0 (see Figure 3.1), is similar to that reported in the classical work of Khalak and Williamson [14] in that three distinct response branches are discernible. The initial branch was observed within $2.9<U^*<4.9$. The upper branch occurred in the range of $5.0<U^*<6.3$, within which A^* reached a maximum value of 1.14 and the vibration frequency and natural frequency remained close, giving $f^*=1$. The lower branch was found to span the range $6.4<U^*<11.3$. A very similar amplitude response was seen by Klamo et al. [9], who also observed a trend towards linearly decreasing lower branch amplitudes as they increased damping. Within the lower branch, f^* increased from 1 to 1.2, where it remained relatively constant for $U^*>8.5$. Desynchronization was observed beyond $U^*=11.3$, where the cylinder vibrations transition into random motions with small amplitudes. Figure 3.2 shows the displacement trace and the corresponding frequency spectrum of the plain cylinder in the upper branch at $U^*=5.1$. Steady vibrations with nearly constant amplitudes and a dominant peak in the frequency spectrum are observable near lock-in.

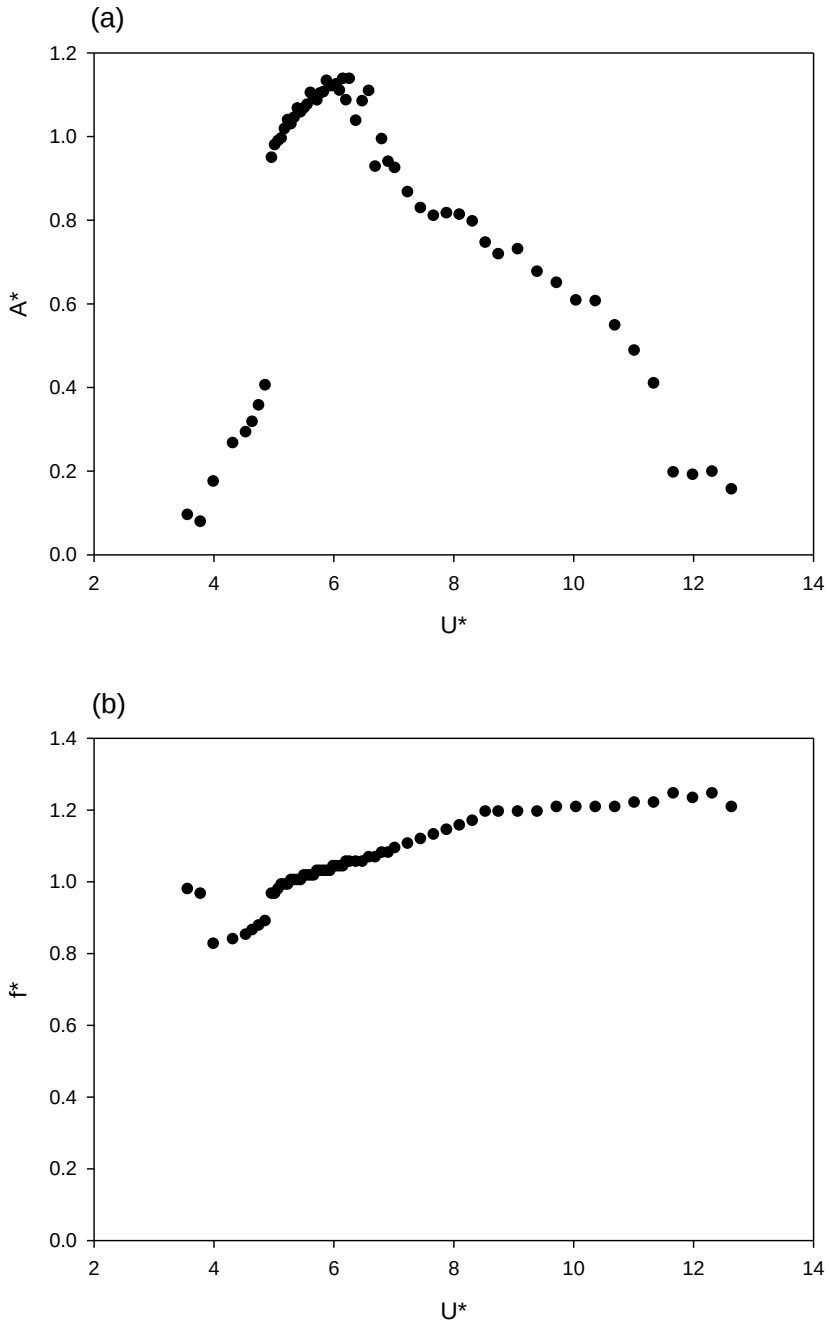

Figure 3.1 (a) Amplitude and (b) frequency response of a plain circular cylinder ($m^*\zeta = 0.015$)

The full strip thickness range in Table 2.1 was tested for the level of damping used in Case 0 to fully assess their effect on the cylinder response. In addition to undergoing VIV at low values of U^*, the response of a cylinder attached with smooth strips transitions to galloping oscillations at higher flow velocities. For all strip thicknesses tested, steady constant-amplitude vibrations are observed coinciding with the upper branch range of Case 0. This is followed by a transition region, leading to a fully-developed galloping response characterized by large-amplitude, steady vibrations and a linear increase in A^* with U^*.

3.1.1 Effect of increasing strip thickness at constant $m^*\zeta$

Case 1, in which the cylinder is fitted with strips measuring 1.6% of its diameter, shows a gradual transition from VIV to galloping. The upper branch decreases very slightly in width and ranges from $5.1<U^*<6.3$. The maximum amplitudes observed in the initial, upper, and lower branches were consistently lower than those of the plain cylinder, matching a result previously measured by Vinod with smooth strips [1]. The lower branch ranges from $6.3<U^*<8.3$, which is a significant decrease in size from the plain cylinder case. Transition to galloping, characterized by non-uniform oscillations, occurs in the velocity range of $8.3<U^*<12.1$. The range $12.3<U^*<15.9$ is observed to have steady vibration amplitudes for each individual test case, and a relatively constant maximum A^*, fluctuating between $A^*=1.33$ and $A^*=1.40$. At $U^*>15.9$, steady oscillations and linearly increasing vibration amplitudes, typical of galloping, were observed. Displacement traces and PSD plots for the upper branch, transition region, and galloping are shown in Figure 3.3. In the upper branch, we see very little variation in amplitude over the test period, as well as one dominant peak frequency. The transition

region shows a reduction in magnitude and uniformity of the amplitude response and a decrease in periodicity of oscillations, reflected in the lack of a dominant peak frequency. During galloping, the system returns to steady, uniform vibration amplitudes with one dominant oscillation frequency with smaller peaks at higher harmonics. These harmonic peaks are observed throughout the galloping response of every case tested, a phenomenon also observed by Park and Bernitsas [23]. Cases 2 through 5, with respective strip thickness ratios of 8.2%, 16.3%, 24.5%, and 31%, have no discernable lower branch and result in A^* increasing with U^* over the entire velocity range. There is also a lack of a clearly identifiable transition region as seen in Case 1. The amplitude response of Cases 0-5 is shown in Figure 3.4a. The upper branch begins between $5.1<U^*<5.3$ for each case, increasing slightly with strip thickness. In Case 2, A^* increases linearly from the start of the upper branch until $U^*=10.2$, where it begins to increase linearly at a faster rate until $U^*=13.7$. At this point, the slope increases again until $U^*=21.3$, the highest flow velocity tested due to structural concerns resulting from significant flutter at the free end of the cylinder. In Case 3, a higher A^* was observed for each U^* compared to the previous cases, reaching the maximum allowable A^* of 4.7 at $U^*=19.1$. The steady response region of the amplitude response of Case 3 increased at an average rate of 0.26 per one unit U^*, whereas Case 2 had a rate of $0.16/U^*$, marking a faster increase in galloping amplitude. After the initial branch, Case 4 showed higher A^* for each value of U^* compared to each of the previous cases. The cylinder reached $A^*=4.7$ at $U^*=14.5$ at an average rate of $0.40/U^*$. Case 5 yielded a max amplitude of $A^*=4.7$ at $U^*=13.2$ at an average rate of $0.47/U^*$, a modest increase from the previous case. Figure 3.5 shows the average slope of the steady response section of A^* vs. U^* for each strip thickness.

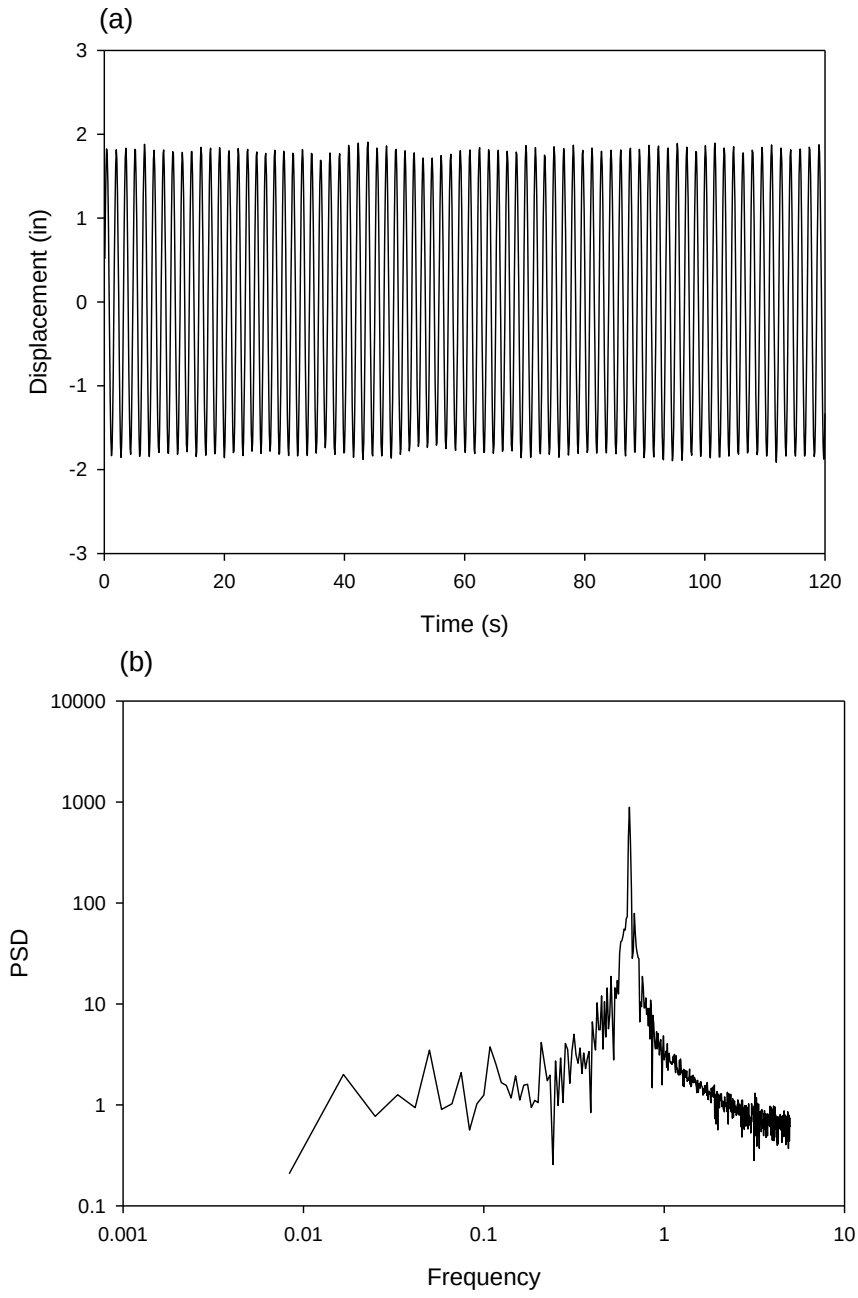

Figure 3.2 (a) Displacement trace and (b) frequency spectrum during synchronization of a cylinder without strips

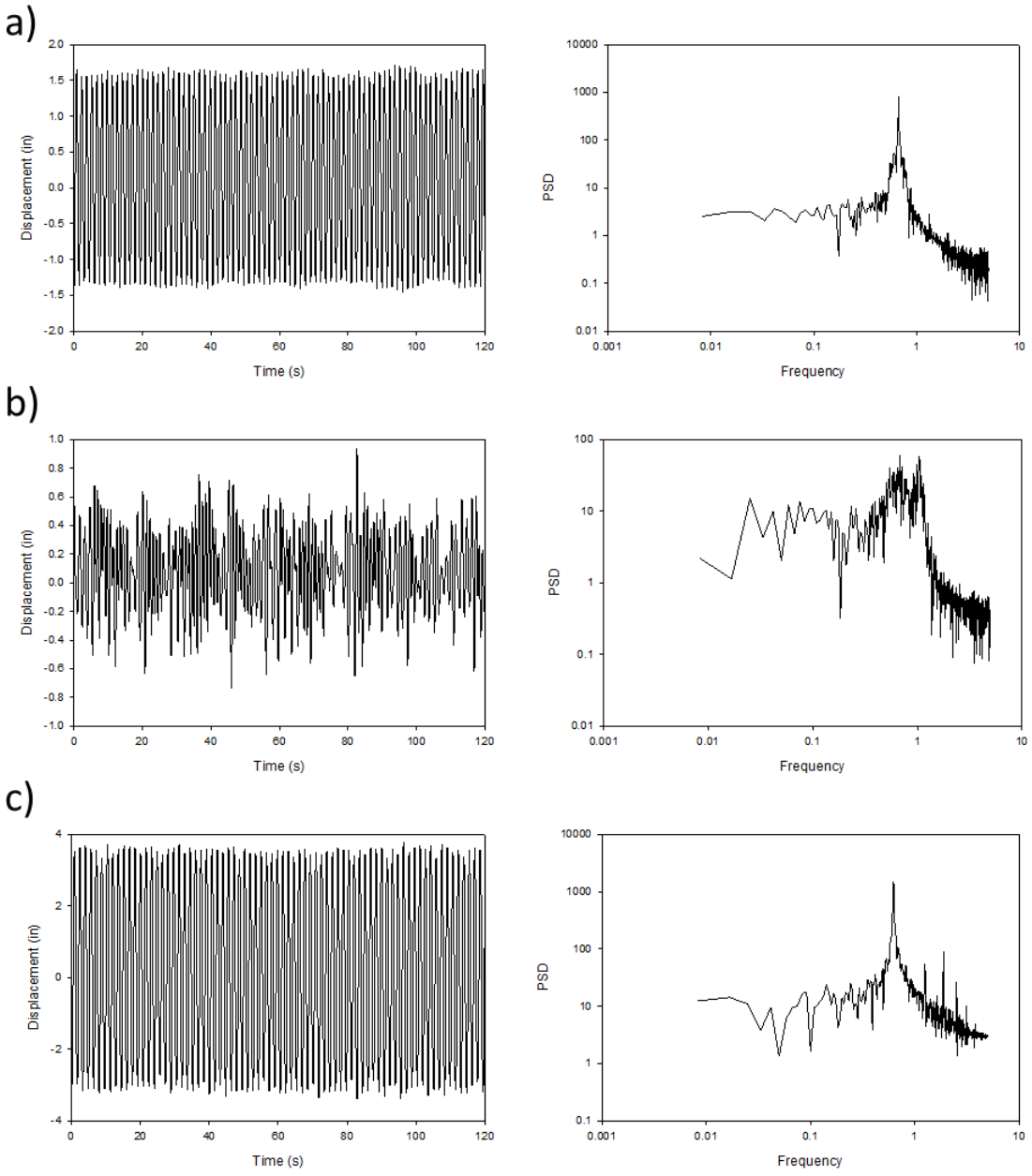

Figure 3.3 Displacement trace and frequency spectrum for Case 1 (H/D = 1.6%) for (a) upper branch (b) VIV-galloping transition (c) galloping

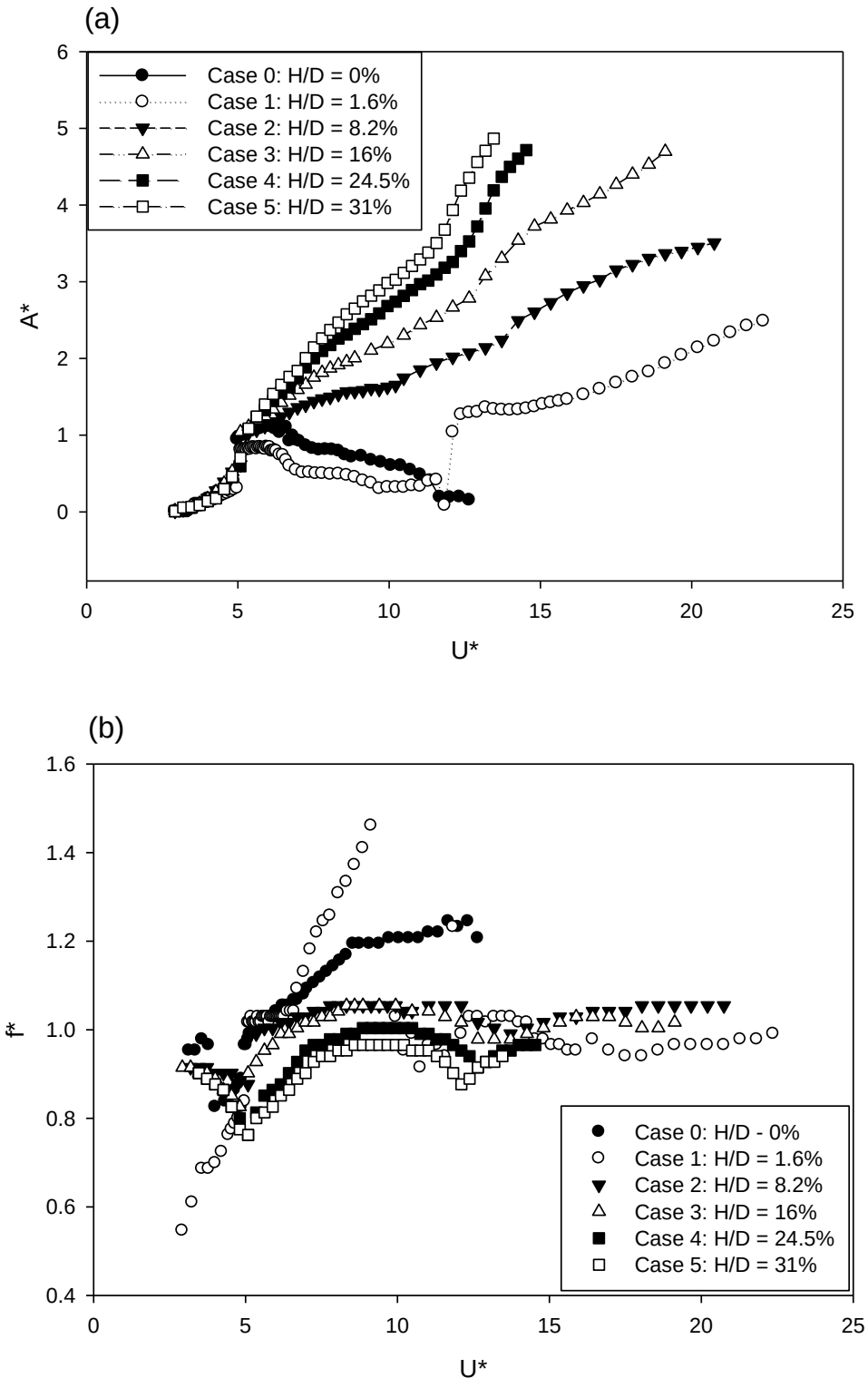

Figure 3.4 (a) Amplitude response and (b) frequency response for all cases at $m^*\zeta = 0.015$

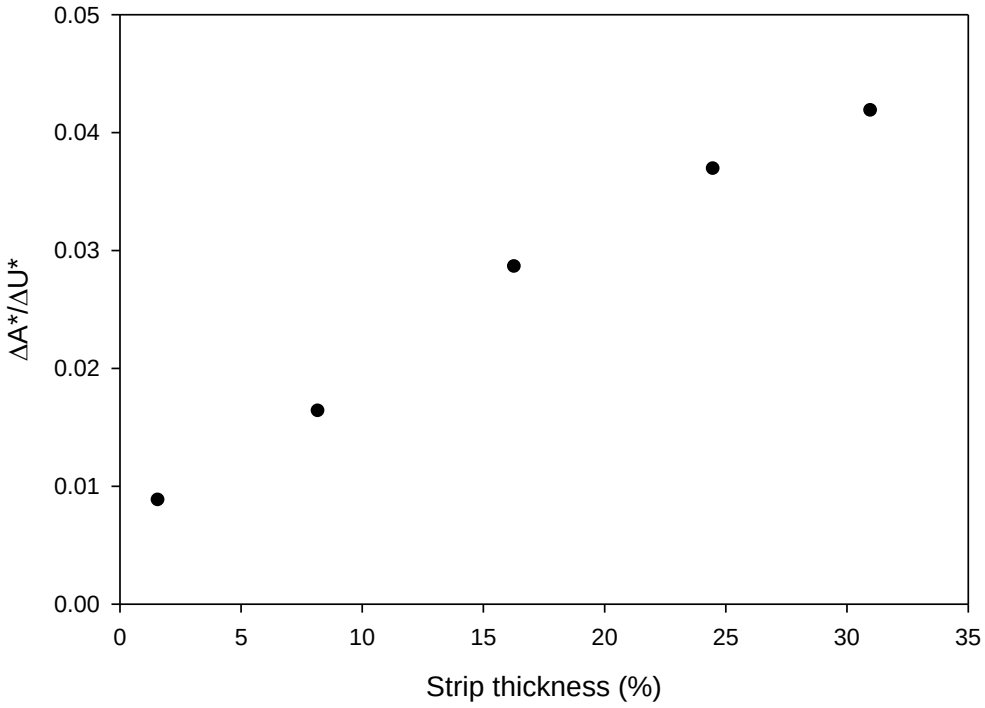

Figure 3.5 Rate of increase of A* with U*

The oscillation frequency gradually increases over the steady vibration regime for all strip cases and is similar to the response observed for a smooth cylinder, as seen in Figure 3.4b. In the steady vibration regime, lower f^* values are observed with increasing strip thickness at a given U^*. Case 1 experienced f^* values very close to 1 for the entire upper branch until U^*=6.6. For the rest of the steady vibration regime, which spanned until U^*=8.3, f^* increased linearly to a value of 1.33, higher than observed in Case 0. The dominant frequency continued to increase for part of the transition region until U^*=9.7, where f^* reached its maximum at 1.51, although the peaks became less prominent. For the remainder of the transition region, the frequency spectrum plots did not have strong dominant peaks, so fluctuations in f^* were observed. Beyond U^*=13.2, f^* remained close to 1. In Case 2, f^* increased to 1.05 over 5.3<U^*<9.9. It fell to a local minimum at U^*=13.7 and then rose back to unity with increasing U^*. In Case 3, we observed a similar rise in f^* from the onset of steady amplitude vibrations until U^*=9.9. In the range 9.9<U^*<13.7, f^* again decreased to a local minimum, after which it increased gradually to a value of 1.03 at maximum amplitude. For Case 4, f^* increased from 0.81 at U^*=5.3 to 1.00 at U^*=10.2. It fell to a minimum frequency, lower than that of the previous cases, at U^*=12.6 and then approached unity until the cylinder reached maximum amplitude. In Case 5, f^* increased to 0.97 by U^*<10.2. The lowest drop in frequency of all previous cases, f^*=0.88, occurred at U^*=12.4, after which it increased to f^*=0.94 at maximum amplitude. Overall, the frequencies observed in galloping decreased with increasing strip thickness, with the exception of the 1.6% strip thickness case.

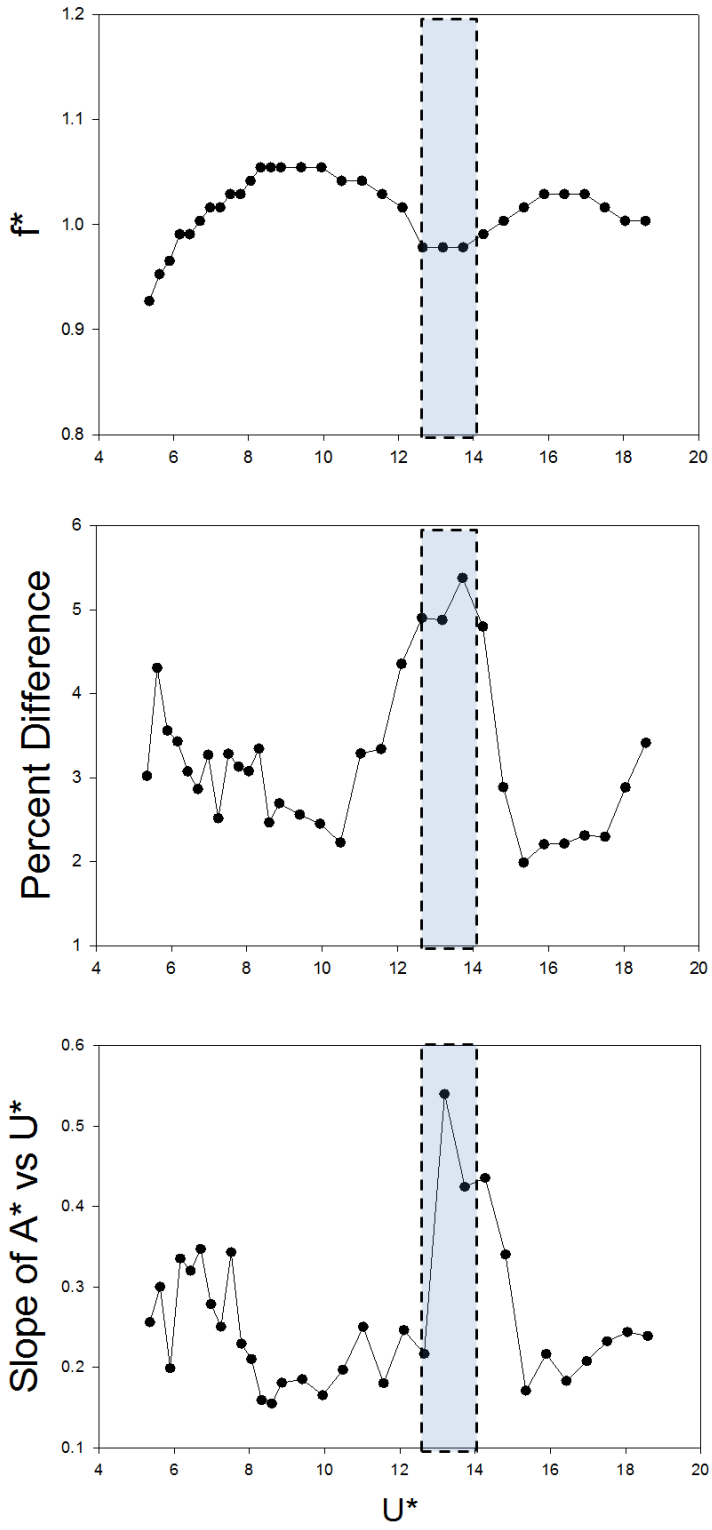

Figure 3.6 Comparison of (a) frequency spectrum; (b) percent difference in top 10% and r.m.s. amplitudes, and (c) slope of A* vs. U* for the steady vibration regime for Case 3 (H/D = 16.3%)

The common trend seen in Cases 2-5 is that the location of the local minimum frequency in each case corresponds to an increase in slope of the amplitude response. This point in each case is also shown to have higher levels of fluctuation in the amplitude response than the surrounding regions. This phenomenon is shown in Figure 3.6. Fluctuation was measured in terms of percent difference between the top 10% average amplitude and r.m.s. amplitude in a given displacement trace. This unsteady behavior is typically observed during transition between VIV and galloping. The increase in slope and increased unsteadiness, followed by linearly increasing amplitudes characteristic of galloping, indicates that the frequency drop is located within the transition regime.

3.1.2 Effect of mass-damping at constant strip thickness

Six additional cases were tested to observe the effect of mass-damping on the amplitude and frequency response. Two higher levels of mass damping, $m^*\zeta = 0.026$ and $m^*\zeta = 0.075$, were tested for the plain cylinder and strip thickness ratios of 8.2% and 24.5%. For the plain cylinder (see Figure 3.7 and Figure 3.8), increasing mass-damping is shown to result in lower upper-branch amplitudes, as well as upper and lower branches spanning smaller *Re* ranges. The lower branch was shown to decrease steadily in amplitude for each case, deviating from the behavior seen by Williamson [14] where a large, nearly constant-amplitude lower branch was observed. The rate of decline of the lower branch was also faster for lower $m^*\zeta$. These observations support those seen by Lee and Bernitsas [15] where they varied damping while maintaining a constant spring stiffness. As $m^*\zeta$ increased, the transition from the initial branch to the upper branch occurred at slightly lower U^*. Lower $m^*\zeta$ resulted in a longer upper branch with continuously increasing amplitudes followed by a significant drop at the start of the lower

branch. The range of synchronization also occurs at lower *Re* as mass-damping increases but spans roughly the same U^* range. These observations are consistent with the trends seen by Lee and Bernitsas in their constant damping, varying stiffness experiments [15]. As $m^*\zeta$ increases, the maximum peak frequency achieved over the entire velocity range, occurring in the lower branch, decreases. It can be seen that f^* remains close to 1 in the upper branch regardless of flow speed.

At a strip thickness ratio of 8.2%, A^* increases for the entire range of U^* for all $m^*\zeta$. Higher mass-damping resulted in steady amplitude vibrations at lower Reynolds numbers, as well as a higher slope of A^* vs. *Re*, as shown in Figure 3.9a. At the *Re* where Case 9 reached the maximum allowable A^* of 4.7, Case 8 reached 2.06, and Case 2 reached 1.47. However, the amplitude response as a function of reduced velocity shows the three cases mostly overlapping. Higher $m^*\zeta$ cases saw earlier transition from the initial branch and slightly higher amplitudes throughout the response. As seen in Figure 3.9b, there is an increase in slope of A^* vs. U^* for each case, occurring in the range $13<U^*<14$. As observed with the low damping cases discussed in the previous section, the increase in slope corresponds to a local minimum in the frequency response and a peak in unsteadiness of the corresponding displacement trace. This indicates that the point lies within the transition regime and that the linear amplitude response that follows can be assumed to be fully-developed galloping. Figure 3.10 shows all three cases have an f^* around 1 at the for the first steady vibration region. In each case, the frequency falls to a local minimum below 1 at $13<U^*<14$ and then increases until the end of the test range. The maximum peak frequency attained during galloping was found to increase with decreasing $m^*\zeta$.

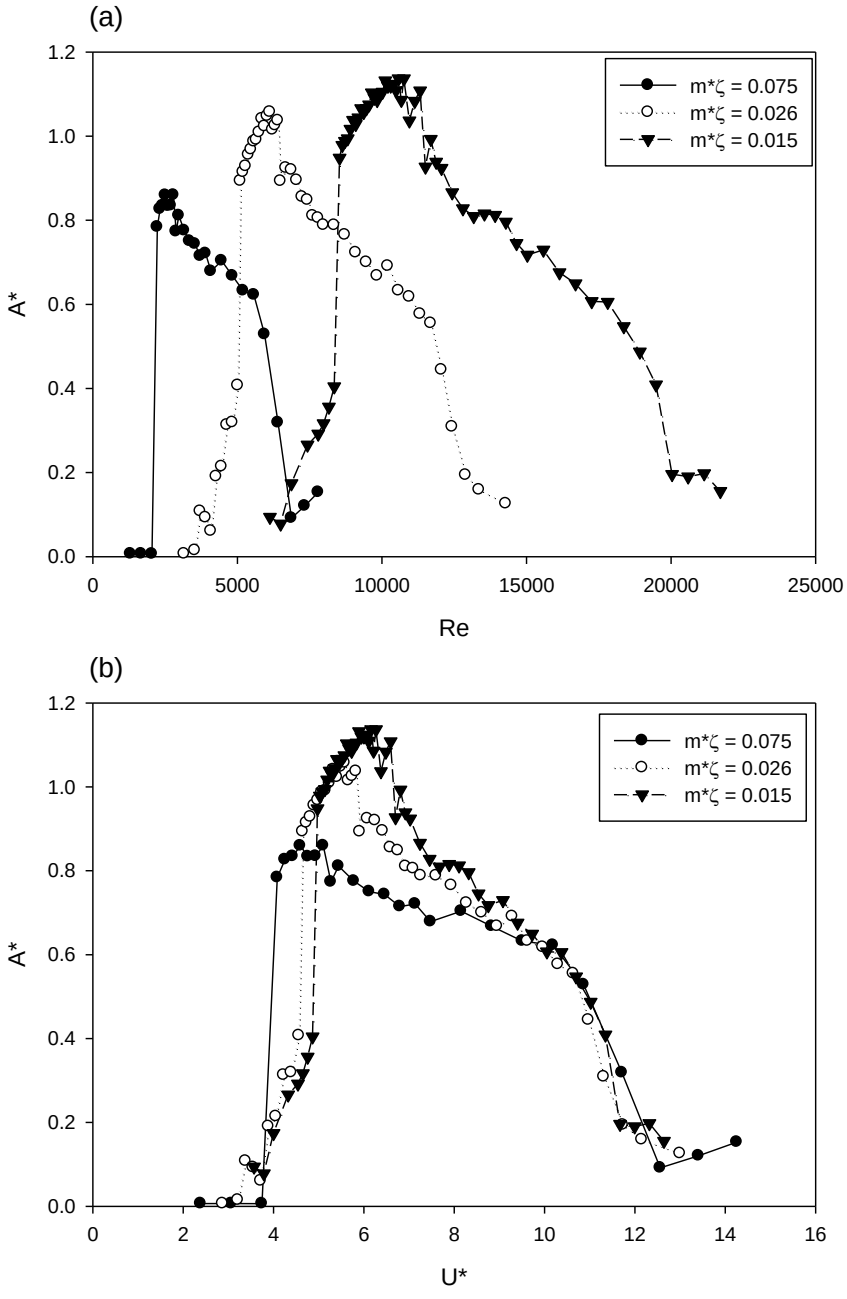

Figure 3.7 Amplitude response of plain cylinders at various mass-damping plotted against (a) Reynolds number and (b) reduced velocity

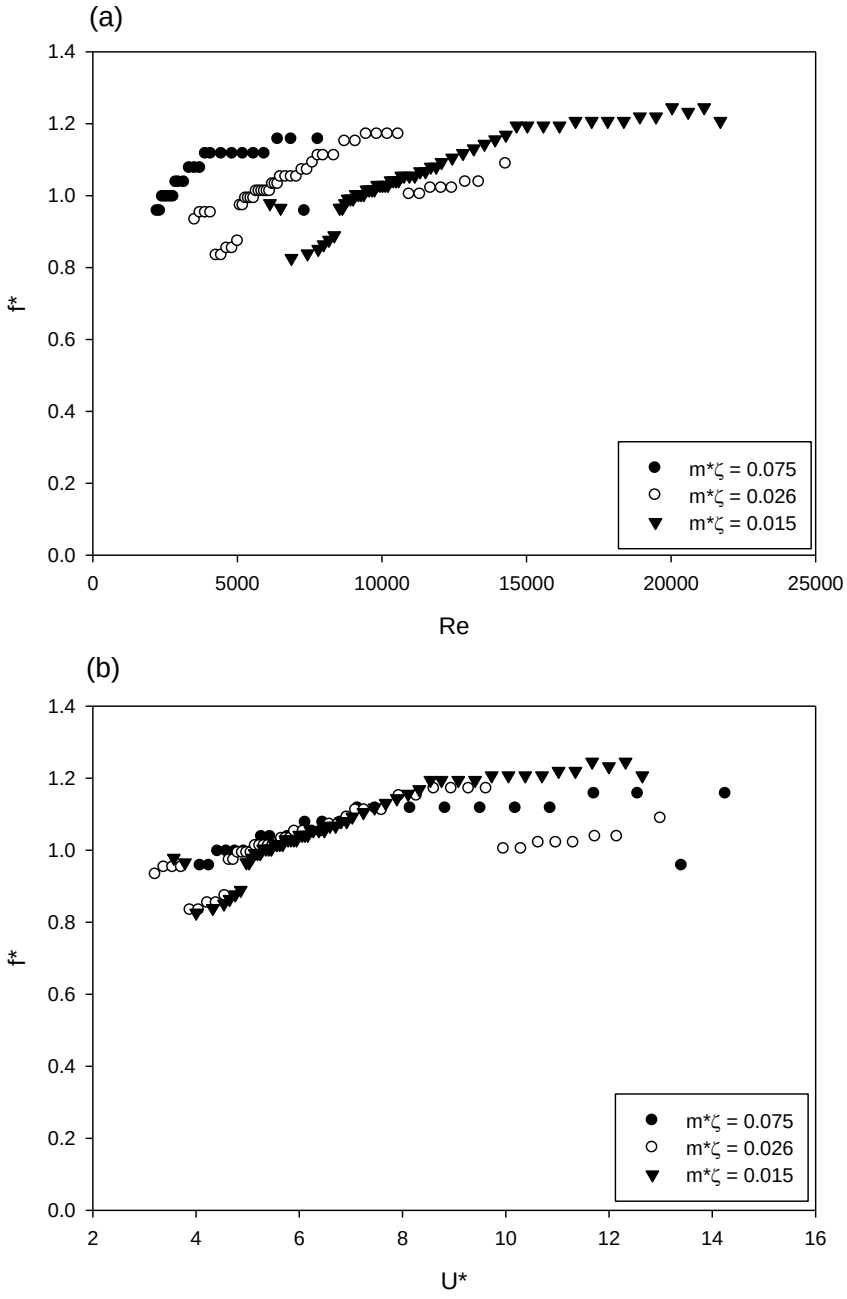

Figure 3.8 Frequency response of plain cylinders at various mass-damping plotted against (a) Reynolds number and (b) reduced velocity

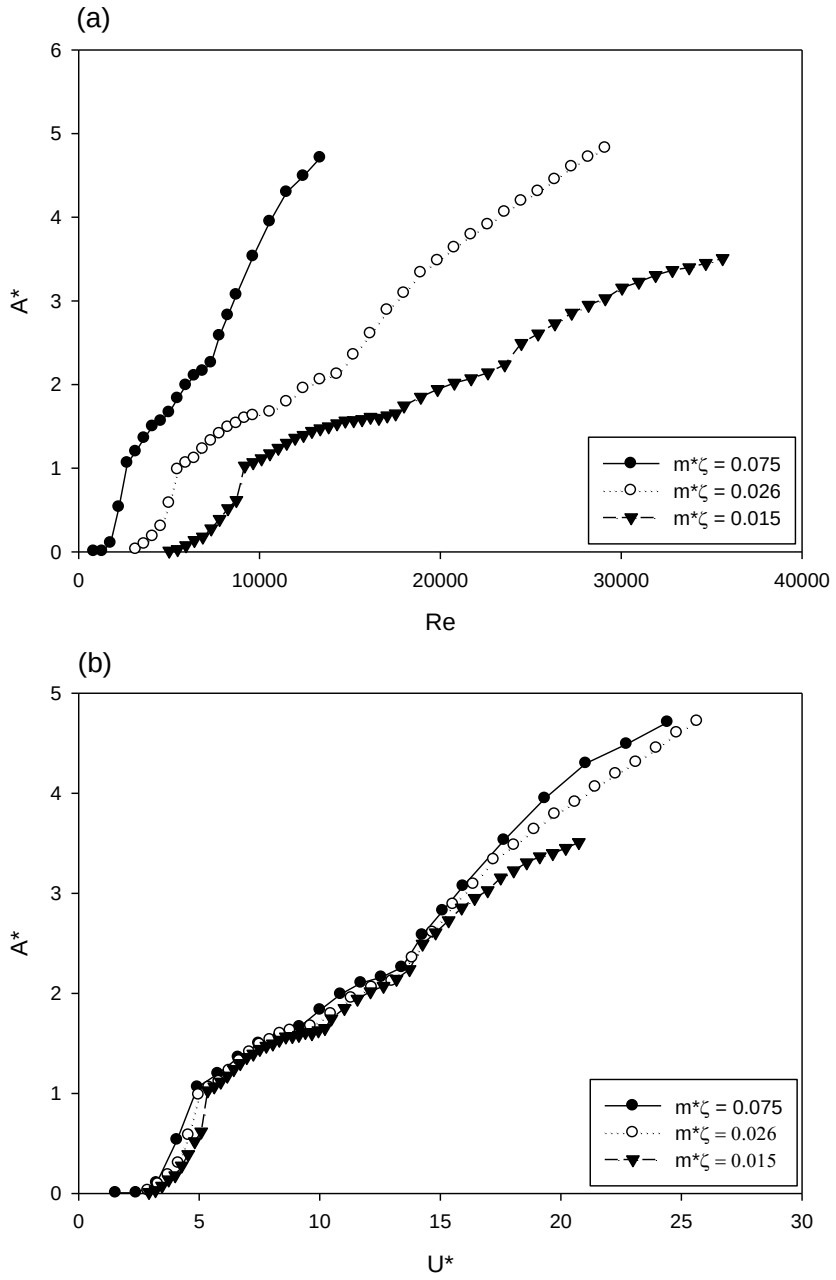

Figure 3.9 Amplitude response of cylinders with strip thickness H/D = 8.2% at various mass-damping plotted against (a) Reynolds number and (b) reduced velocity

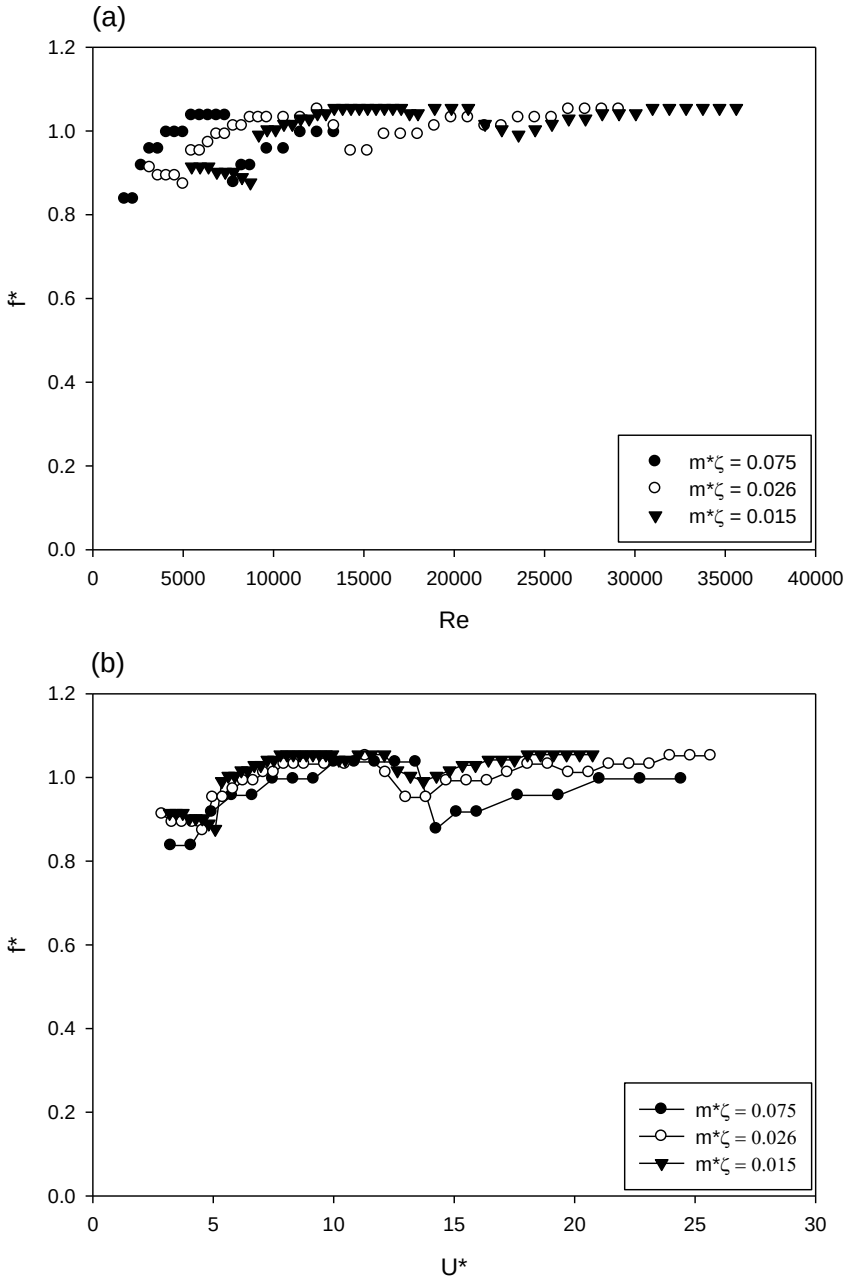

Figure 3.10 Frequency response of cylinders with strip thickness H/D = 8.2% at various mass-damping plotted against (a) Reynolds number and (b) reduced velocity

Similar results were observed with a strip thickness equal to 24.5% of the cylinder diameter, seen in Figure 3.11 and Figure 3.12. The rate of increase of A^* with Re is higher as mass-damping increases, and the maximum allowable A^* is achieved at lower flow velocities. When plotted against reduced velocity, the response for each case nearly overlaps. Higher mass-damping is shown to result in earlier transition from the initial branch, higher amplitudes throughout, and slightly lower frequencies throughout the response. The change in slope of the amplitude response again coincides with a dip in frequency and increase in displacement trace variability. For the three cases discussed here, this point occurs between $11<U^*<13$, increasing slightly with decreasing $m^*\zeta$. The displacement trace for this point in Case 11 with $m^*\zeta=0.075$ is shown in Figure 3.13. The extreme unsteadiness shows that transition from VIV to galloping is occurring at this point, indicating that the corresponding inflection point in each case lies somewhere within the VIV-galloping transition regime.

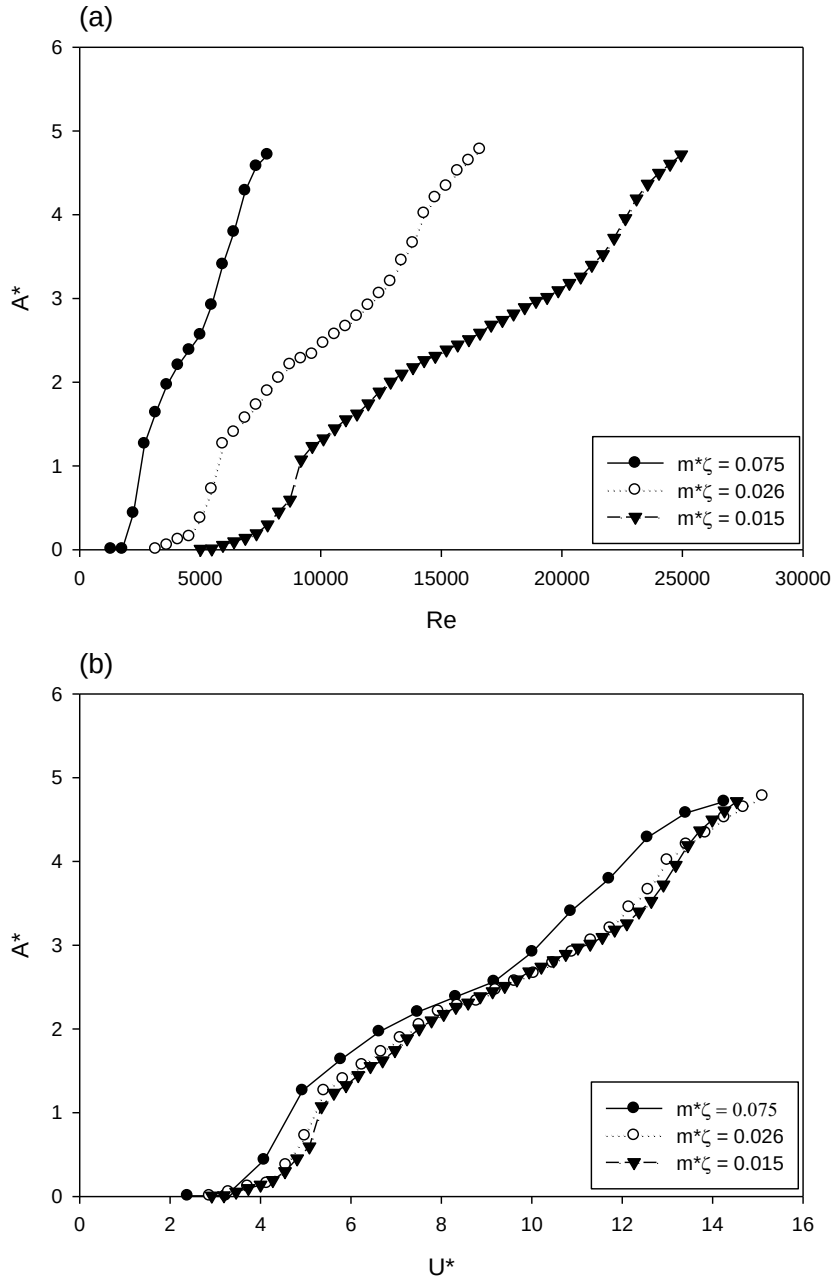

Figure 3.11 Amplitude response of cylinders with strip thickness H/D = 24.5% at various mass-damping plotted against (a) Reynolds number and (b) reduced velocity

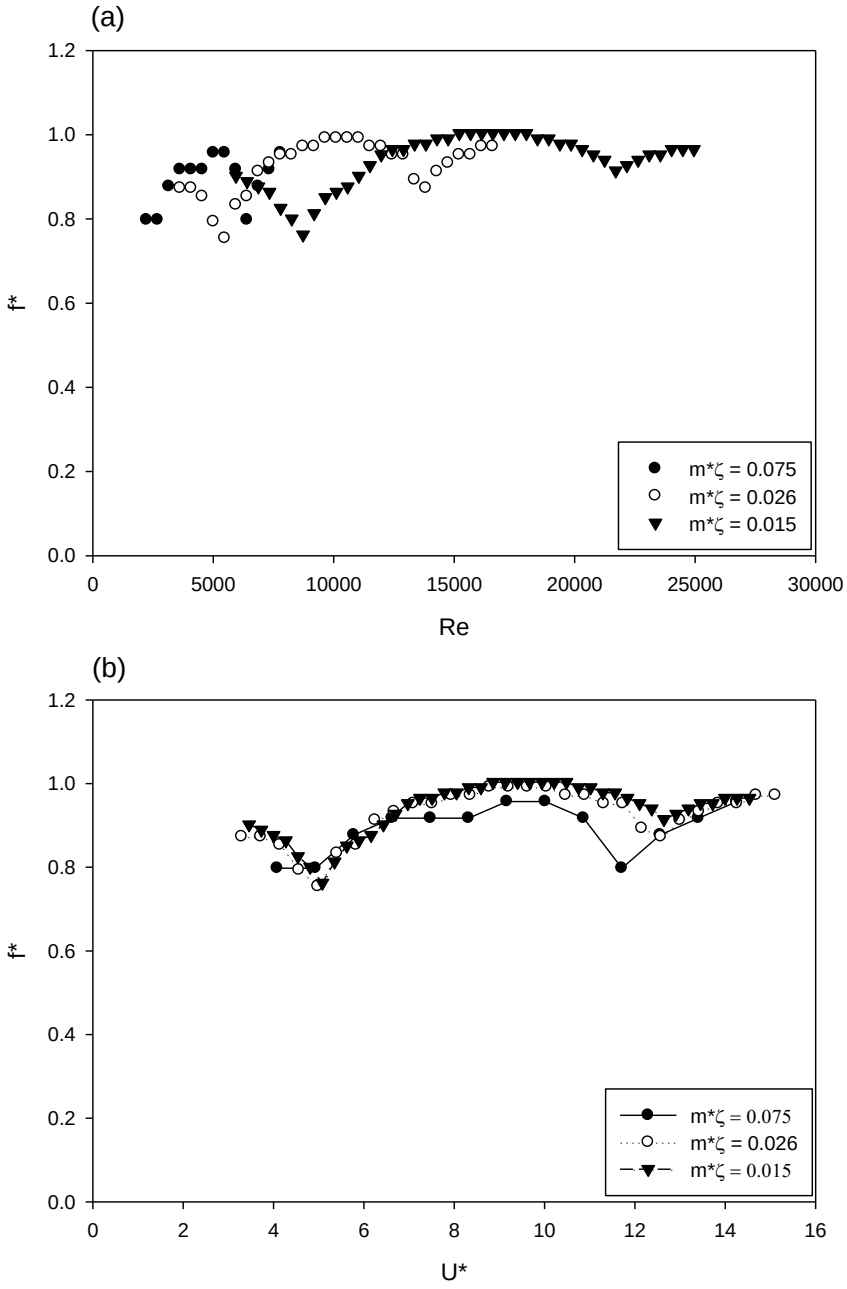

Figure 3.12 Frequency response of cylinders with strip thickness H/D = 24.5% at various mass-damping plotted against (a) Reynolds number and (b) reduced velocity

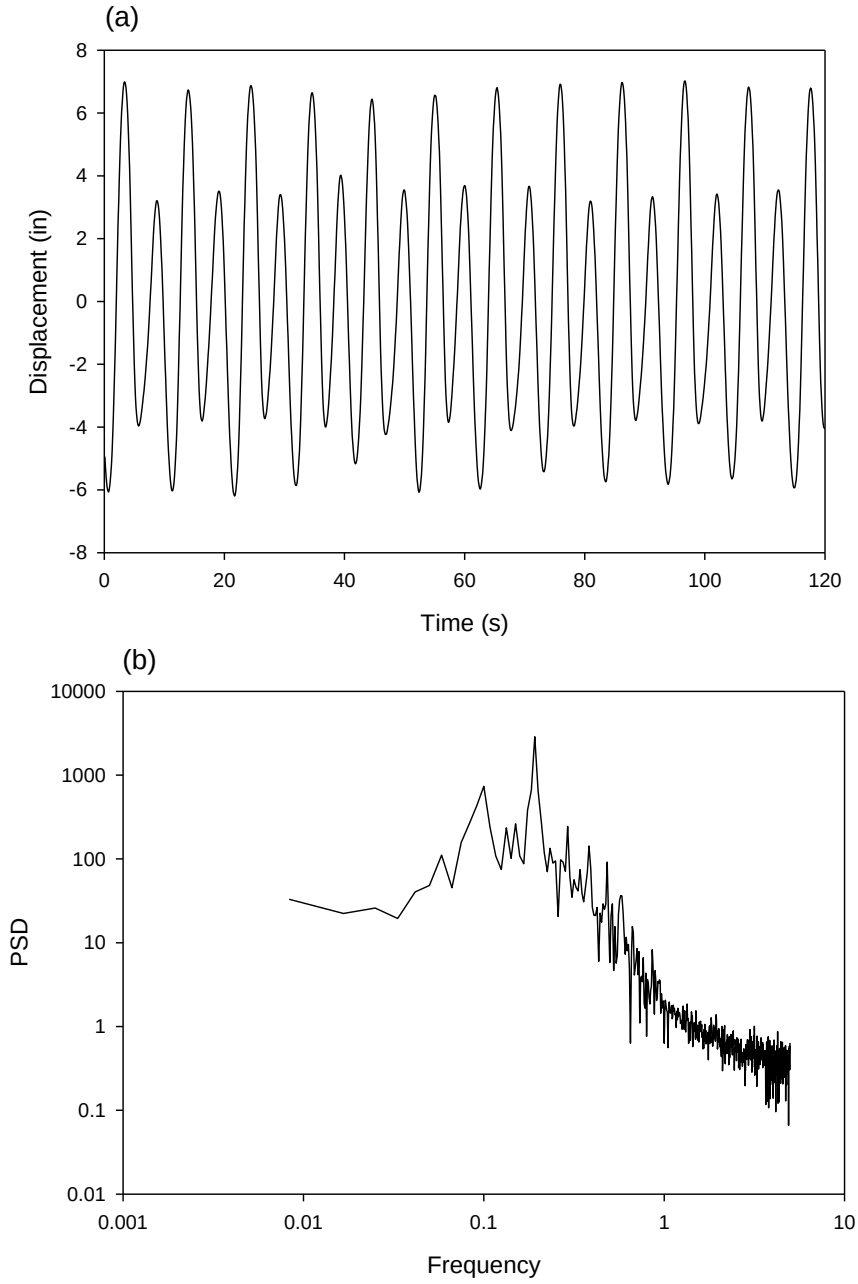

Figure 3.13 (a) Displacement trace and (b) frequency spectrum for Case 11 at $U^* = 11$

3.2 Power Extraction Potential

For a mass-spring-damper system, similar to the one employed in the current work, the total mechanical power can be estimated using the equation:

$$P_{mech} = \frac{1}{T_{cyl}} \int_0^{T_{cyl}} C_{total} \dot{y}^2 dt \tag{8}$$

The power harnessed by such a system depends on the instantaneous oscillation velocities reached with the different strip thickness and mass-damping configurations. A higher oscillation velocity indicates the capability of enhanced power extraction from the flow. To qualitatively assess the power extraction potential of the various tested configurations, we take a closer look at their respective oscillation velocities. The V^2_{rms} observed in Cases 0-5 over the full test range of U^* is plotted in Figure 3.14. The velocity response of these cases bears a trend similar to that of the corresponding amplitude response. Thicker strips led to greater oscillation velocities over most of the flow speeds tested, with the exception of Case 1. For the plain cylinder, Case 0, the maximum V^2_{rms} attained was 0.0223 m^2/s^2, occurring within the upper branch. A comparable V^2_{rms} greater than 0.01 m^2/s^2 but lower than the upper branch value was seen over most of the lower branch. The plain cylinder completely loses its power extraction capability with desynchronization. Case 1 reached a peak V^2_{rms} of 0.0124 m^2/s^2 in the VIV upper branch, almost half of the maximum in Case 0. In the transition regime, it fell below 0.001 m^2/s^2, then reached a maximum of 0.1168 m^2/s^2 at U^*=22.4, the highest flow velocity tested. Cases 2 through 5 increase in V^2_{rms} over the entire range of U^* tested, similar to the trend seen in A^* vs. U^*. Case 2 reached a max V^2_{rms} of 0.262 m^2/s^2 at U^*=20.7. Cases 3 through 5 reached a maximum V^2_{rms} of about 0.4 m^2/s^2 at U^* values of 18, 14.5, and 13.5 respectively. The velocity response also showed an increase in slope coinciding with the

same locations as the amplitude response curves. Increasing the mass-damping of the system in Cases 6 through 11 had a significant impact on the oscillation velocities experienced. Plain cylinder cases 0, 6, and 7 reached a peak V^2_{rms} of 0.0223, 0.0074, and 0.0013 m^2/s^2 in their respective upper branches, indicating higher upper branch power extraction potential for lower mass-damping systems. In Cases 8 and 9, with strip thickness of 8.2%, V^2_{rms} increased over the entire test range of U^* at respective rates of 0.0084 m^2/s^2 and 0.0019 m^2/s^2 per unit U^*, well below 0.015 $m^2/s^2/U^*$ for the low mass-damping case. A similar trend was seen for a thickness ratio of 24.5% for low, medium, and high damping (Cases 4, 10, and 11) where V^2_{rms} increased at rates of 0.042, 0.017, and 0.004 m^2/s^2 per unit U^*. For $m^*\zeta = 0.026$, the 8.2% and 24.5% strip thickness cases reached a V^2rms of 0.17 m^2/s^2 at a U^* of 24 and 15.1 respectively. The same cases under high damping reached V^2_{rms}=0.04 at respective U^* values of 22.7 and 14.3, indicating increased power generation potential with increasing strip thickness regardless of damping. Figure 3.15 shows V^2_{rms} vs. U^* for all 11 test cases.

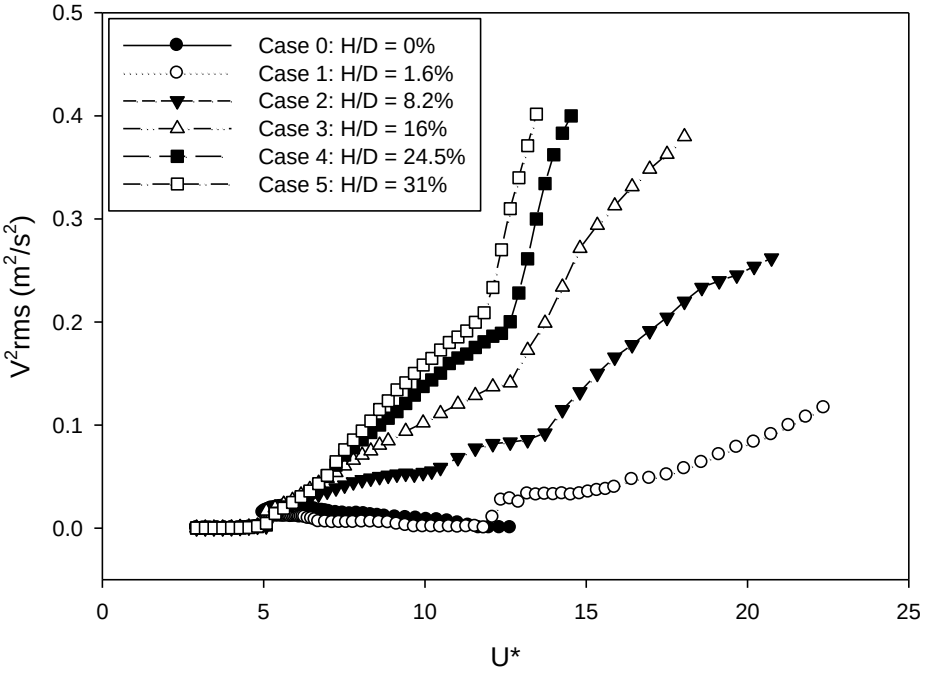

Figure 3.14 V^2_{rms} vs. U^* observed for varying strip thickness at $m^*\zeta = 0.0015$

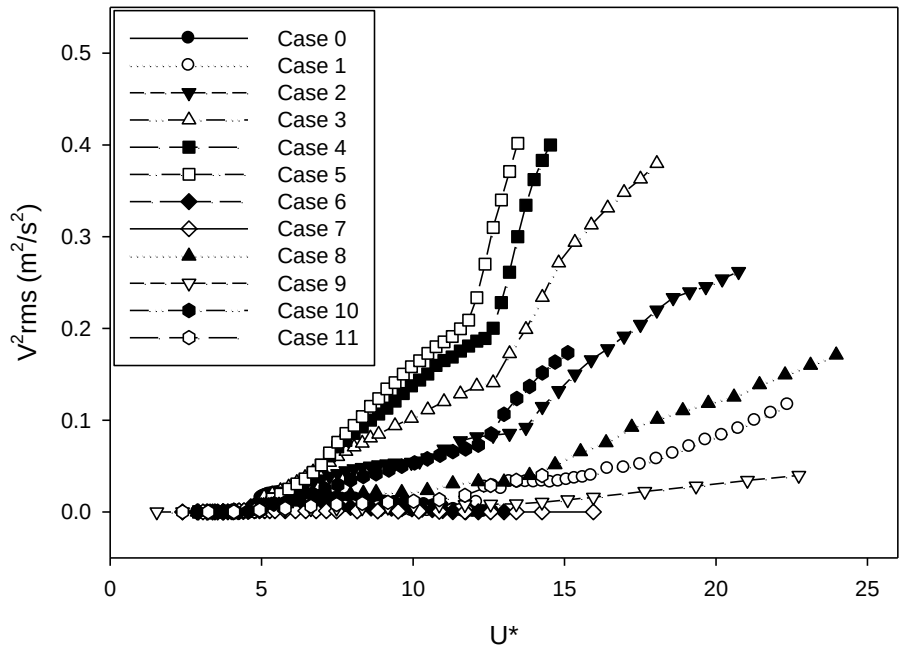

Figure 3.15 V^2_{rms} vs. U^* observed for all cases

The ability of the strips to incite galloping oscillations in addition to VIV significantly expands the flow velocity ranges over which energy extraction is possible. Table 3.1 presents U^* and Re ranges corresponding to each case over which energy extraction is higher than or comparable to the case of a smooth circular cylinder at $m^*\zeta = 0.015$. In this base case, the operating range is the shortest and extends between $5<U^*<11.3$, corresponding to the upper and lower branches. Cases 1 – 11, which lead to galloping oscillations, can harness energy over a velocity range that is theoretically semi-infinite. In Case 1, the operating velocity range is discontinuous due to the presence of a transition regime where the unsteadiness in motion is significant. Cases 2-5 have no discontinuity in operating range, meaning they can all operate from roughly $U^*=5.1$ up to theoretically infinitely high flow velocities. Cases 8-11 can operate at velocities $U^*=5$ and above, showing that altering the mass-damping of the system does not have a significant effect on the reduced velocity where upper branch vibrations begin.

In order to compare the power extraction potential of the different tested cases within their respective operating ranges, we use a non-dimensional parameter, Maximum Power Enhancement Factor, defined as the ratio of the mechanical power attained using a particular cylinder configuration at a given flow velocity to the maximum power extracted using a plain cylinder without strips (Case 0).

$$Max\_PEF = \frac{P_{mech,cylinder+strips}}{MaximumP_{mech,smoothcylinder}} \tag{9}$$

Table 3.1 Theoretical operating regimes for each strip thickness and damping case

Case #	$m^*\zeta$	**H/D (%)**	**Operating *U**** **Range**	**Operating *Re* Range**
0	0.015	0	$5.0<U^*<11.3$	8500-10700
1		1.6	$5.1<U^*<16.11$ $U^*>30.83$	8700-19800, >20800
2		8.2	$U^*>5.3$	>9200
3		16.3	$U^*>5.1$	>8700
4		24.5	$U^*>5.3$	>9200
5		31	$U^*>5.3$	>9200
6	0.026	0	$4.6<U^*<5.8$	5100-6400
7	0.075		$4.1<U^*<5.1$	2200-2800
8	0.026	8.2	$U^*>5.0$	>5500
9	0.075		$U^*>4.9$	>2700
10	0.026	24.5	$U^*>5.4$	>5900
11	0.075		$U^*>4.9$	>2700

Comparing to the maximum power the smooth cylinder case is done to eliminate the dependence on the synchronization regime of the plain cylinder. Therefore, Max-PEF values indicate the improvement in energy extraction potential when compared to the best performance of the smooth cylinder configuration. Max-PEF obtained in all cases are presented in Figure 3.16. In Case 0, Max-PEF values remain close to 1 in the range $5<U^*<6.3$, which corresponds to the upper branch of the smooth cylinder. The Max-PEF of Case 1 is significantly lower than Case 0 until the galloping regime. Within $5.1<U^*<6.3$, Max-PEF observed in Case 1 is lower than the corresponding values observed in Case 0, varying between 0.47 and 0.56. With the onset of galloping oscillations beyond $U^*\sim12.4$, Max-PEF increases from ~1.2 at $U^*=12.4$ to 5.2 around $U^*=22.4$. As strip thickness increases in Cases 2 through 5, Max-PEF greater than 1 are seen at U^* ranging from 5.9 to 6.2. The highest Max-PEF reached in Case 2 is 11.7, significantly higher than the previous case. Cases 3-5 reached Max-PEF of 18 at a U^* of 18, 14.5, and 13.5 respectively. A mass-damping of $m^*\zeta = 0.026$ led to Max-PEF of 0.36 for the plain cylinder, a substantial decrease from Case 0. The two strip cases (8.2% and 24.5%) at this damping reached a Max-PEF of 8.4 at $U^*=24$ and $U^*=15.1$ respectively. The plain cylinder under high damping had a very low Max-PEF of 0.092 in the upper branch. The 8.2% and 24.5% strip thickness cases reached a Max-PEF of 2.8 at U* of 22.7 and 14.3.

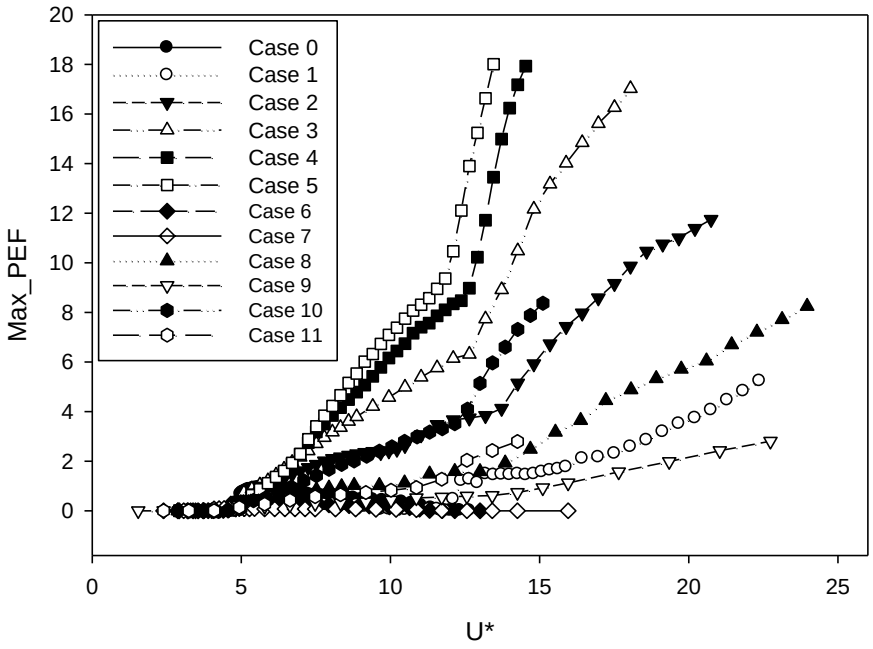

Figure 3.16 Max-PEF of all cylinder configurations

4 Conclusions

The experimental results presented illustrate the effect of strip thickness and mass-damping on FIM of circular cylinders, with strips attached at a location experimentally verified to be beneficial for vibration augmentation. The main findings are summarized below.

- A pair of smooth strips with a thickness as low as 1.6% of the cylinder diameter is capable of inciting high-amplitude galloping oscillations at high flow velocities in addition to inducing lower amplitude VIV at low flow velocities.
- The maximum allowable amplitude with the current experimental setup, A^*=4.7, was reached in all strip cases other than Cases 1 and 2, at a pace increasing with strip thickness. At a strip thickness of 31% with low mass-damping (Case 0), the A^* limit was reached at a U^* of 13.5, where Cases 1-4 had reached A^* values of 1.3, 2.2, 3.3, and 4.2 respectively.
- As mass-damping was increased, both VIV and galloping were observed at significantly lower Reynolds numbers. With smooth cylinders, higher $m^*\zeta$ resulted in lower VIV upper branch amplitudes. However, A^* increased more rapidly in the galloping regime *as* $m^*\zeta$ was increased, reaching higher amplitudes at much lower flow speeds. Sun et al. [24] saw the rate of increase in A^* with both U^* and *Re* to be relatively constant with increasing damping but decreased with increasing spring stiffness. The results seen here may be an effect of the coupled nature of stiffness and damping in the setup.
- Each strip case had a prominent increase in slope in its amplitude response, which seems to correspond to transition to fully-developed galloping. This phenomenon

occurred at varying values of U^* for Cases 1-5 at constant damping but occurred at approximately the same U^* for a fixed strip thickness regardless of damping.

- For all cases with and without strips, the VIV regime, or onset of steady vibrations, had $f^* \sim 1$. With the exception of Case 1, increasing strip thickness was observed to result in lower galloping frequencies for $m^*\zeta = 0.015$. As $m^*\zeta$ was increased, the maximum frequency in the galloping regime decreased slightly for a given strip thickness.

- The estimated values of V^2_{rms} show that the oscillation velocities of the cylinder attached with strips are greater than those of the plain cylinder case. For a particular flow velocity, higher strip thickness leads to higher oscillation velocities indicating better energy extraction capabilities. This trend was verified using the estimated Max-PEF's.

- Attaching a circular cylinder with thick strips at 60° from the frontal stagnation point not only increases the energy extraction capability at a particular flow velocity but also significantly increases the range of flow velocities over which energy can be harnessed.

References

1. Vinod, A. and A. Banerjee, *Surface protrusion based mechanisms of augmenting energy extraction from vibrating cylinders at Reynolds number 3×10^3–3×10^4*. Journal of Renewable and Sustainable Energy, 2014. **6**(6): p. 063106.
2. Morgenthal, G., *Fluid Structure Interaction in Bluff-body Aerodynamics and Long-span Bridge Design: Phenomena and Methods*. 2000: University of Cambridge, Department of Engineering Cambridge.
3. Zdravkovich, M.M., *"Flow Around Circular Cylinders, Volume1: Fundementals," Oxford University Press, Oxford, U.K.,*. 1997.
4. Norberg, C., *Flow around a circular cylinder: Aspects of fluctuating lift.* Journal of Fluids and Structures, 2001. **15**: p. 459-469.
5. Williamson, C.H.K. and A. Roshko, *Vortex formation in the wake of an oscillating cylinder.* Journal of Fluids and Structures, 1988. **2**(4): p. 355-381.
6. Khalak, A. and C.H.K. Williamson, *Motions, forces and mode transitions in vortex-induced vibrations at low mass-damping.* Journal of Fluids and Structures, 1999. **13**(7-8): p. 813-851.
7. Meneghini, J. and P. Bearman, *Numerical simulation of high amplitude oscillatory flow about a circular cylinder.* Journal of Fluids and Structures, 1995. **9**(4): p. 435-455.
8. Lienhard, J.H., *Synopsis of Lift ,Drag and Vortex Frequency Data for Rigid Circular Cylinders*. 1966, Washington State University: Pullman, WA.
9. Klamo, J., A. Leonard, and A. Roshko, *The effects of damping on the amplitude and frequency response of a freely vibrating cylinder in cross-flow.* Journal of Fluids and Structures, 2006. **22**: p. 845-856.
10. Sarpkaya, T., *Vortex-induced oscillations. A selective review.* Journal of Applied Mechanics, 1979. **46**: p. 241-258.
11. Sarpkaya, T., *A critical review of the intrinsic nature of vortex-induced vibrations.* Journal of Fluids and Structures, 2004. **19**: p. 389-447.
12. Williamson, C.H.K. and R. Govardhan, *Vortex-induced vibrations.* Annual Review of Fluid Mechanics, 2004. **36**: p. 413-455.

13. Bearman, P., *Circular cylinder wakes and vortex-induced vibrations.* Journal of Fluids and Structures, 2011. **27**(5): p. 648-658.
14. Khalak, A. and C.H.K. Williamson, *Fluid forces and dynamics of a hydroelastic structure with very low mass and damping.* Journal of Fluids and Structures, 1997. **11**(8): p. 973-982.
15. Lee, J.H. and M.M. Bernitsas, *High-damping, high-Reynolds VIV tests for energy harnessing using the VIVACE converter.* Ocean Engineering, 2011. **38**(16): p. 1697-1712.
16. Sun, H., et al., *Virtual Spring–Damping System for Flow-Induced Motion Experiments.* Journal of Offshore Mechanics and Arctic Engineering, 2015. **137**(6): p. 061801.
17. Raghavan, K. and M. Bernitsas, *Experimental investigation of Reynolds number effect on vortex induced vibration of rigid circular cylinder on elastic supports.* Ocean Engineering, 2011. **38**(5): p. 719-731.
18. Mannini, C., A.M. Marra, and G. Bartoli, *VIV–galloping instability of rectangular cylinders: Review and new experiments.* Journal of Wind Engineering and Industrial Aerodynamics, 2014. **132**(0): p. 109-124.
19. Weaver, D. and I. Veljkovic, *Vortex shedding and galloping of open semi-circular and parabolic cylinders in cross-flow.* Journal of Fluids and Structures, 2005. **21**(1): p. 65-74.
20. Alonso, G., et al., *On the galloping instability of two-dimensional bodies having elliptical cross-sections.* Journal of Wind Engineering and Industrial Aerodynamics, 2010. **98**(8): p. 438-448.
21. Assi, G.R. and P.W. Bearman, *Transverse galloping of circular cylinders fitted with solid and slotted splitter plates.* Journal of Fluids and Structures, 2015. **54**: p. 263-280.
22. Chang, C.C., R.A. Kumar, and M.M. Bernitsas, *VIV and galloping of single circular cylinder with surface roughness at $3.0\times10^4 \le Re \le 1.2\times10^5$.* Journal of Ocean Engineering, 2011. **38**: p. 1713-1732.

23. Park, H., R.A. Kumar, and M.M. Bernitsas, *Enhancement of flow-induced motion of rigid circular cylinder on springs by localized surface roughness at* $3\times10^4 \leq Re \leq 1.2\times10^5$. Ocean Engineering, 2013. **72**(0): p. 403-415.
24. Sun, H., et al., *Effect of mass-ratio, damping, and stiffness on optimal hydrokinetic energy conversion of a single, rough cylinder in flow induced motions.* Renewable Energy, 2016. **99**: p. 936-959.
25. Parkinson, G. and P. Sullivan, *Galloping response of towers.* Journal of Wind Engineering and Industrial Aerodynamics, 1979. **4**(3-4): p. 253-260.
26. Novak, M. and A.G. Davenport, *Vibration of towers due to galloping of iced cables.* ASCE Journal of Engineering Mechanics Division, 1978. **104**: p. 457.
27. Bokaian, A. and F. Geoola, *Flow-induced vibrations of marine risers.* Journal of Waterway, Port, Coastal, and Ocean Engineering, 1987. **113**(1): p. 22-38.
28. Zdravkovich, M.M., *Review and classification of various aerodynamic and hydrodynamic means for suppressing vortex shedding.* Journal of Wind Engineering and Industrial Aerodynamics, 1981. **7**: p. 145-189.
29. Scruton, C. and D.E.J. Walshe, *A menans for avoiding wind excited oscillations of structures with circular or nearly circular cross section.* Natl. Phys. Lab. (U.K), Aero Rep.335: Br. Pat. 907,851, 1957.
30. Nakagawa, K., et al. *An experimental investigation of aerodynamic instability of circular cylindersat supercritical Reynolds numbers*. in *Proc. 9th Jpn, Congr. Appl. Mech*. 1959. Tokyo.
31. Mahrenholtz, O. and H. Bardowicks, *Aeroelastic problems at masts and chimneys.* Journal of Wind Engineering and Industrial Aerodynamics, 1979. **4**(3-4): p. 261-272.
32. Price, P., *Suppression of the fluid-induced vibration of circular cylinders.* Journal of the Engineering Mechanics Division, 1956. **82**(3): p. 1-22.
33. Zdravkovich, M.M. *Flow induced vibrations in irregular tube bundles and their suppression*. in *Proceedings of International Symposium on Vibration Problems in Industry*. 1973. National Physics Lab, U.K.

34. Zdravkovich, M.M. and J.R. Volk, *Effect of shroud geometry on pressure distribution around a cicular cylinder.* Journal of Sound and Vibration, 1972. **20**: p. 451-455.
35. Zdravkovich, M.M. *Circular cylinder enclosed in varioius shrouds*. in *American Society of Mechanical Engineering and Vibration*. 1971. Toronto.
36. Wong, H.Y. *An aerodynamic means of suppressing vortex induced oscillations*. in *Proc. Inst. Civ. Eng.,*. 1977.
37. Baird, R.C., *Wind Induced Vibration of a pipe line suspension bridge and its cure.* Proc. Inst. Civ. Eng.,, 1955. **77**: p. 797-804.
38. Roshko, A., *On the wake and drag of bluff bodies.* Journal of Aeronautical Sciences, 1955. **22**: p. 124-132.
39. Grimminger, G., *The effect of rigid guide vanes on the vibration and drag of a towed circular cylinder.* David Taylor Model Basin, Washington, Rep. 504, 1945.
40. Park, H., R.A. Kumar, and M.M. Bernitsas, *Suppression of vortex-induced vibrations of rigid circular cylinder on springs by localized surface roughness at* $3\times10^4 \leq Re \leq 1.2\times10^5$. Ocean Engineering, 2016. **111**: p. 218-233.
41. Sui, J., et al., *VIV suppression for a large mass-damping cylinder attached with helical strakes.* Journal of Fluids and Structures, 2016. **62**: p. 125-146.
42. Dhanak, M.R. and N.I. Xiros, *Springer Handbook of Ocean Engineering*. 2016: Springer.
43. Jacobson, P., *Assessment and mapping of the riverine hydrokinetic resource in the continental United States*. 2012, Electric Power Research Institute (EPRI), Palo Alto, CA (United States).
44. Bernitsas, M.M. and K. Raghavan, *VIVACE(Vortex Induced Vibration Aquatic Clean Energy): A New Concept in Generation of Clean and Renewable Energy from Fluid Flow.* Journal of Offshore Mechanics and Arctic Engineering, 2008. **130**(4): p. 041101.
45. Bernitsas, M.M. and K. Raghavan, *Enhancement of Vortex Induced Forces and Motion through Surface Roughness Control*, U.S.P.a.T. Office, Editor. 2011.
46. Raghavan, K. and M.M. Bernitsas. *Enhancement of High Damping VIV through Roughness Distribution for Energy Harnessing at* $8\times10^3 < Re < 1.5\times10^5$. in

Proceedings of ASME 27th International Conference on Offshore Mechanics and Arctic Engineering. 2008. Estoril, Portugal.

47. Kim, E.S., M.M. Bernitsas, and R. Ajith Kumar, *Multicylinder Flow-Induced Motions: Enhancement by Passive Turbulence Control at 28,000≤Re≤120,000.* Journal of Offshore Mechanics and Arctic Engineering, 2013. **135**(2): p. 021802-021802.

48. Govardhan, R. and C. Williamson, *Defining the 'modified Griffin plot'in vortex-induced vibration: revealing the effect of Reynolds number using controlled damping.* Journal of Fluid Mechanics, 2006. **561**: p. 147-180.

Appendix

A. LVDT Support Assembly

The LVDT setup had gone through a major redesign before the present design was developed. Initially, the core rod-extension rod assembly was mounted to the traversing plate, and the LVDT body was mounted on the corner of the frame of the test apparatus. This proved ineffective because the extension rod length required was too high, leading to significant sag in the core rod assembly which created too much friction for proper operation. Damping tests showed that a much higher level of frictional damping occurred during the direction of motion illustrated in Figure A.1a.

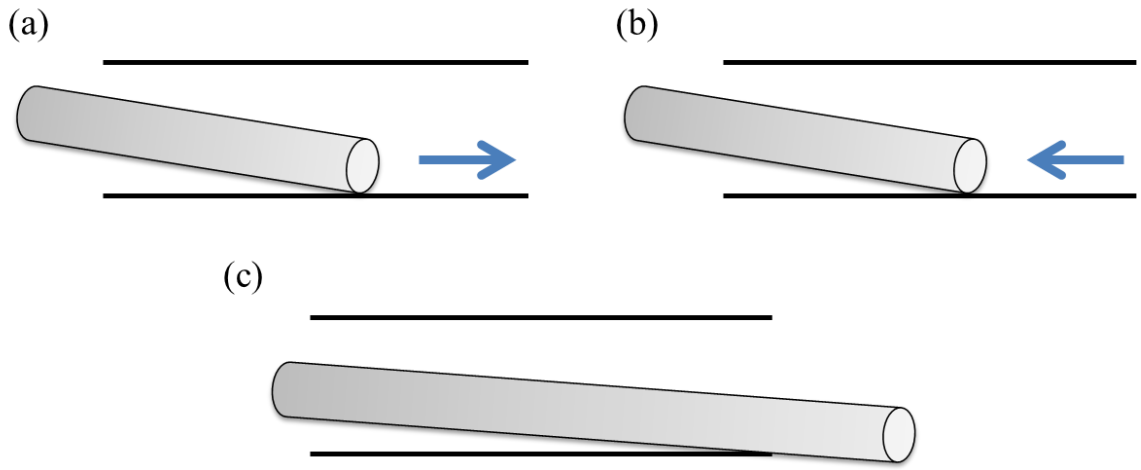

Figure A.1 Interaction of core rod and bottom inner surface of LVDT body in the first design iteration [(a) and (b)] and second design iteration (c)

In an attempt to combat this, an extension was attached to the other end of the core rod so that the contact in Figure A.1a would be eliminated (Figure A.1c). This showed marginal improvement but was ultimately ineffective due to the excessive overhang of the core rod assembly.

The next concept involved manufacturing a new traversing plate with long extensions on either side on which to mount supports for the core rod assembly. This

would prevent sag on one end by having both sides supported and would reduce the necessary length of the core rod assembly. This concept was never taken to the design phase because the extended plate design was thought to be too bulky and cumbersome. However, this led to the final design presented in this report where the core rod was supported on both sides of the frame, and the LVDT body was mounted to the traversing plate.

B. LVDT Setup and Calibration

The LVDT was purchased from Macro Sensors, a subsidiary of TE Connectivity. The linearity tolerance on the core rods and extension rods supplied by Macro Sensors was too high to allow frictionless operation for a model of this size, even when properly aligned. The bore diameter is 0.235" and the core rod diameter is 0.188", giving a clearance of about 0.024" which was too tight of a tolerance over the 60" core/extension rod system. Instead of using the extension rods from Macro Sensors, which were of the same diameter as the core rod and attachable via #4-40 set screws, I used #4-40 threaded rods as extensions. The smaller diameter gave more clearance which allowed for better alignment with less friction. These rods are also very flexible due to their small diameter, enabling them to be pulled taut to decrease the linearity error.

Alignment was performed in a 3 step process:

1. Align the front face of each mount to be perfectly perpendicular to the LVDT. This was done by fixing the mount loosely in place and sliding the steel shaft (parallel to the LVDT) until contact was made. The front face was aligned flush to the end of the shaft and tightened into place.
2. Slide the plate all the way to one side and center the core rod on the LVDT body. Slide the plate to the other side and repeat.
3. Slide the plate along the shafts and listen for rubbing or scraping sounds. Watch how the alignment changes and adjust if the core rod hits the sides of the bore at any point along the length.

C. Electronics

The LVDT was powered by a 3.3 A, 24 VDC National Instruments power supply model PS-14. The data acquisition system, a National Instruments model USB-6003, has an 8 terminal analog input with a USB output. The LVDT body has input and output wires, as well as a power common wire. A wiring diagram is shown below:

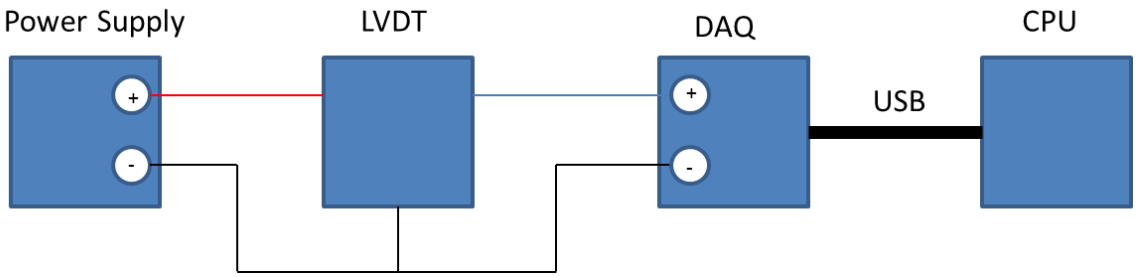

Figure C.1 Wiring diagram for DAQ

D. Data Acquisition

A LabVIEW VI (Figure D.1) was developed in LabVIEW 2012 to facilitate data acquisition. The DAQ Assistant, shown in Figure D.2, command was used to link the USB-6003 DAQ. The input signal range was set to the LVDT output range of -10V to +10V. Experimental data was collected in individual runs lasting 2 minutes which equates to 1200 samples at a sampling rate of 10 Hz. The data is exported as a .lvm file as shown in Figure D.3. Dragging and dropping the .lvm data file into an open Microsoft Excel worksheet neatly formats the time and displacement data collected and allows it to be resaved as a .xlsx file.

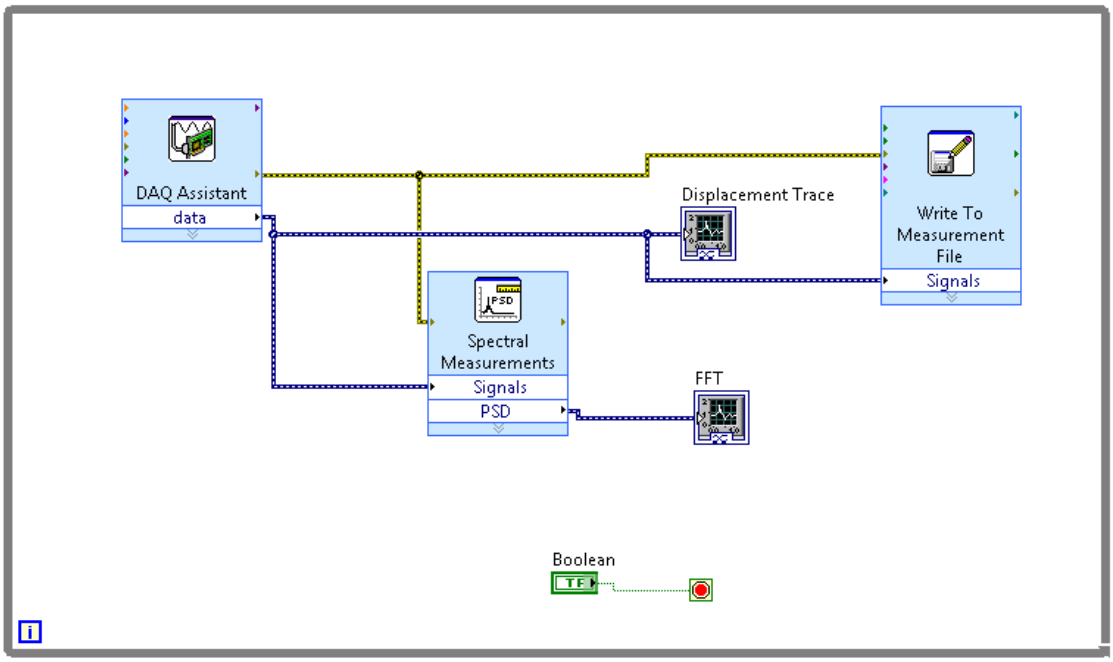

Figure D.1 LabVIEW VI used to acquire LVDT data

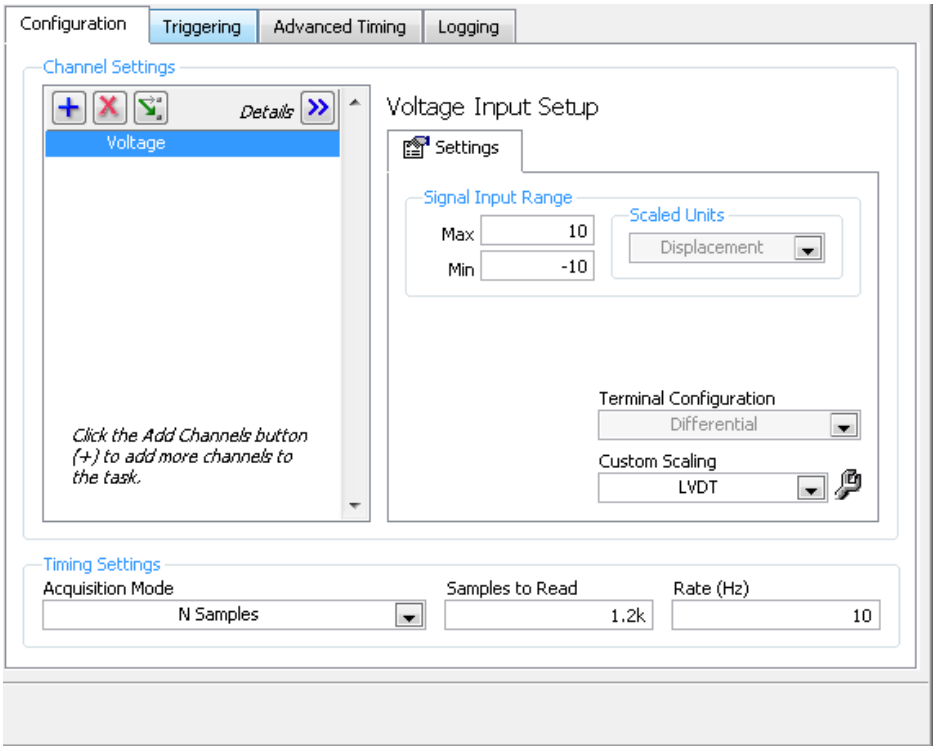

Figure D.2 DAQ Assistant setup

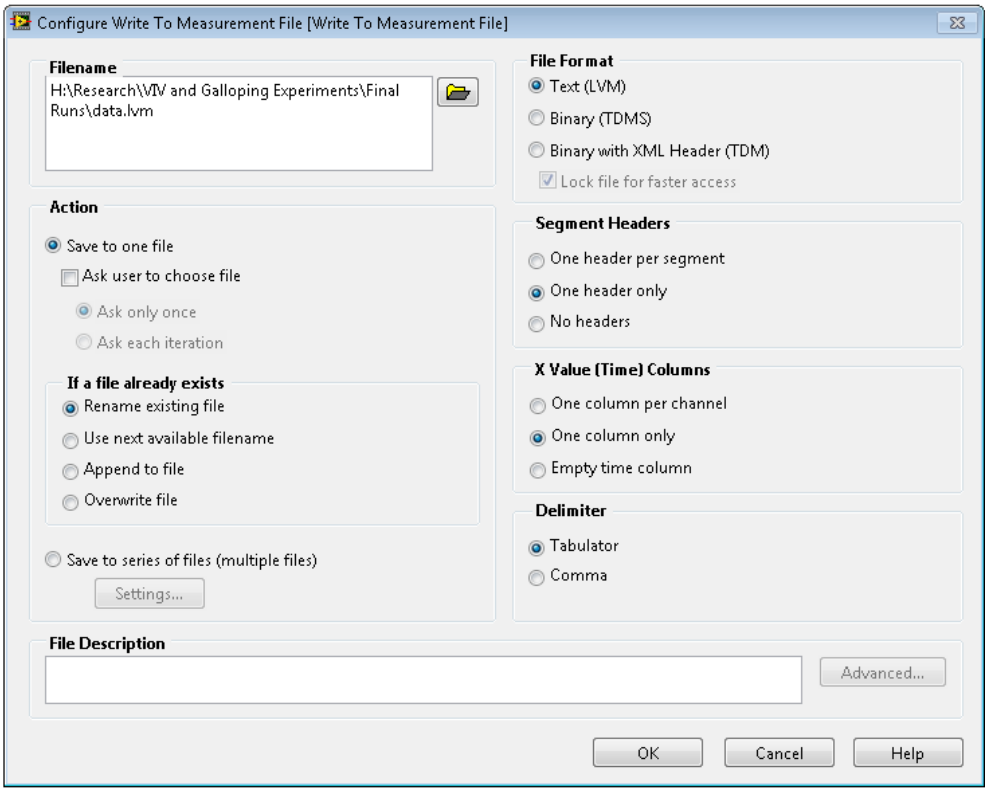

Figure D.3 Configuration of settings to export and save data acquired through LabVIEW

E. MATLAB Codes

E.1 Displacement Trace

```
clc;
clear;

disp = xlsread('12p2hz','B24:B1223');
disp = disp' - 10.983;

num_of_files = numel(disp);
time = 0.1:0.1:num_of_files/10;

% Plot displacement trace
plot(time,disp,'-')

% Plot frequency spectrum
[F,X] = FFT(disp,time);
figure
loglog(F,X)

amplitudes = finding_amplitudes(disp);

sorted_amplitudes = sorting(amplitudes);

total_average = sum(sorted_amplitudes)/length(sorted_amplitudes)

top_10 = 0.1*length(sorted_amplitudes);

top_20 = 0.2*length(sorted_amplitudes);

for z = 1:top_10
    filter_10(z) = sorted_amplitudes(z);
end

for y = 1:top_20
    filter_20(y) = sorted_amplitudes(z);
end

top_10_average = sum(filter_10)/length(filter_10)

top_20_average = sum(filter_20)/length(filter_20)

%%% Power Calculation ------------------------------------------------
---

dispm = disp*0.0254;

%%% Finding the velocity at each time step

vel = zeros(1,length(time));
```

```
for i = 2:length(time)
    vel(i) = (dispm(i)-dispm(i-1))/(time(i)-time(i-1));
end

save('results.mat')
Arms = rms(amplitudes)
Drms = rms(disp);
Vrmssq = (rms(vel))^2
rmsdata = [top_10_average,Arms,Drms,Vrmssq];
xlswrite('RMS Values.xlsx',rmsdata)
```

E.2 Damping Test

```
clc;
clear;
figure

disp = xlsread('damping2_1_24','B24:B323');
disp = disp';
disp = disp - 10.973;
numtime = numel(disp);

for j = 1:numtime
    time(j) = (j-1)/10;
end

plot(time,disp,'-')
title('Displacement History')
xlabel('Time in Seconds')
ylabel('Displacement')

spring_k = 84.4;    % N/m
mass = 4.79;    % kg
n = length(disp);

for start = 1:n
    if disp(1,start) ~= disp(1,start+1)
        break;
    end
end
if disp(1,start+1) >= disp(1,start)
    direction = 1;       % If direction is 1 then curve starts going
upward
else
    if disp(1,start+1) < disp(1,start)
        direction = 2;   % If direction is 2 then curve starts going
downward
    end
end

p = 1;
if direction == 1      % Curve starts Going up from begining
    flag = 1;
    for i = start:n-1
        if flag == 1    % It is going up
            if disp(1,i+1) < disp(1,i)
            record(p) = disp(1,i);
            p = p+1;
            flag = 0;
            end
        end
        if flag == 0    % It is going down
            if disp(1,i+1) > disp(1,i)
               record(p) = disp(1,i);
               p = p+1;
               flag = 1;
```

```
            end
        end
    end
end
if direction == 2      % Curve starts Going Down from begining
    flag = 0;

    for i = start:n-1

        if flag == 0    % It is going down

            if disp(1,i+1) > disp(1,i)
            record(p) = disp(1,i);
            p = p+1;
            flag = 1;
            end

        end

        if flag == 1    % It is going up
            if disp(1,i+1) < disp(1,i)
               record(p) = disp(1,i);
               p = p+1;
               flag = 0;
            end
        end
    end

end

k = 1;
zeta = zeros(15);
for n = 1:15
    decc = (1/n)*log(record(1)/record(2*n+1));

    zeta(k) = decc/sqrt((4*pi*pi)+(decc)^2);

    C(k) = 2*zeta(k)*sqrt(spring_k*mass);
    k = k+1;

end

avg_damping = mean(C)
avg_zeta = mean(zeta)
```

Vita

Andrew Auvil was born on May 20, 1992, in Macungie, PA. He received his Bachelor of Science degree in Mechanical Engineering from Penn State University in May 2015. During his undergraduate career, he completed engineering internships with Ingersoll Rand and Jack Lehr Electric, Inc. He enrolled at Lehigh University in August 2015 and joined the Turbulent Flows Laboratory in October 2015. Andrew graduated with a Master of Science degree in Mechanical Engineering in May 2017.